Journal of Computational and Applied Mechanics, Vol. 9., No. 2., (2014), pp. 171–199

IN-PLANE BUCKLING OF ROTATIONALLY RESTRAINED HETEROGENEOUS SHALLOW ARCHES SUBJECTED TO A CONCENTRATED FORCE AT THE CROWN POINT

László Kiss
Institute of Applied Mechanics, University of Miskolc
H-3515 Miskolc-Egyetemváros
mechkiss@uni-miskolc.hu

[Received: March 26, 2014]

Abstract. The nonlinear in-plane stability of shallow arches with cross-sectional inhomogeneity is investigated. It is assumed that a central concentrated load is exerted at the crown of the arch and the supports are uniform rotationally restrained pins at the endpoints with constant stiffness. The effects of the springs on the stability is investigated. It is found that such arches may buckle in an antisymmetric bifurcation mode with no strain increment at the moment of the stability loss, and in a symmetric snap-through mode with an increased strain. The effects of the springs are notable on the bucking ranges and also on the critical (buckling) loads. If the spring stiffness is zero we get back the results valid for pinned-pinned arches and as the stiffness of the rotational restraints tends to infinity the results become consistent with those for fixed-fixed arches. The results computed are compared with finite element calculations.

Mathematical Subject Classification: 74G60, 74B15
Keywords: Heterogeneous arch, stability, snap-through, bifurcation, rotational restraint

1. Introduction

Arches are widely used in many engineering applications. Let us mention, for instance, their role in arch bridges and roof structures. It is naturally important to be aware of the behavior of such structural members. An early scientific work on the mechanical behavior of such arches was published in the 19th century by Bresse [1], who derived the connection between the displacements and the inner forces. Regarding the stability, Hurlbrink [2] was the first to work out a model for the determination of the buckling load assuming the inextensibility of the centerline. The model of Chwalla and Kollbrunner [3] accounts for the extensibility of the centerline. Results by Timoshenko and Gere [4] are also of importance. Since the 1960s, work on stability issues became more intensive. Schreyer and Masur provided an analytical solution to arches with rectangular cross-section in [5]. DaDeppo [6] showed first in 1969 that quadratic terms in the stability analysis should be taken into account. Dym in [7] and [8] derives results for shallow arches under dead pressure. The thesis by Szeidl [9] determines the Green's function matrices of the extensible pinned-pinned and fixed-fixed circular

beams and determines not only the natural frequencies but also the critical loads given that the beam is subjected to a radial dead load. Finite element solutions are provided by e.g., Noor [10], Calboun [11], Elias [12] and Wen [13] with the assumption that the membrane strain is a quadratic function of the rotation field. A more accurate model is established by Pi [14]. Analytical solutions for pinned-pinned and fixed-fixed shallow circular arches under a central load are provided by Bradford et al. in [15], [16].

In the open literature there can hardly be found account for elastic supports when investigating the buckling behavior of arches. However, as structural members are often connected to each other, they can provide elastic rotational restraints. This can, in one way, be modeled by applying pinned supports with torsional springs, which impede the end rotations of the arch. Such a hypothesis is used by Bradford et al. in [17] for symmetric supports and a central load and in [18], where the spring stiffnesses are different at the ends. The authors have come to the conclusion that the springs have a significant effect on the in-plane elastic buckling behavior of shallow arches. Stiffening elastic supports for sinusoidal shallow arches are modeled in [19] by Plaut.

Within the frames of the present article a new geometrically nonlinear model is introduced for the in-plane elastic buckling of shallow circular arches with cross-sectional inhomogeneity. Nonlinearities are taken into account through the rotation field. The loading is a concentrated force, normal in direction and exerted at the crown point. The principle of virtual work is used to get the equilibrium equations. Uniform, rotationally restrained pinned supports are considered at the ends by using torsional springs with constant stiffness. The effects of the elastic restraints on the buckling types and buckling loads are studied. Special cases when the spring stiffness is zero and when it tends to infinity coincide with the earlier results in [20], [21] valid for pinned-pinned and for fixed-fixed supports. The solution algorithm is based on the one presented in [17]. However, the current model uses less neglects and is also valid for nonhomogeneous materials. In addition, more accurate predictions for not strictly shallow arches are also a benefit.

The paper is organized in seven Sections. Section 2 presents the fundamental hypotheses and relations for the pre- and post-buckling states. The differential equations, which govern the problem are derived in Section 3. Solutions to these are provided in Sections 4 and 5. Numerical evaluation of the results is presented in Section 6. The article concludes with a short summary, which is followed by the Appendix and the list of references.

2. Fundamental relations

2.1. **Pre-buckling state.** Figure 1 shows the rotationally restrained arch and the applied curvilinear coordinate system, which is attached to the E-weighted centerline (or centerline for short). The former has a constant initial radius ρ_o. The right-handed local base is formed by the unit vectors $\mathbf{e}_\xi$ (tangent to the centerline), $\mathbf{e}_\eta$

(perpendicular to the plane of the centerline) and $\mathbf{e}_\zeta$ (normal to the centerline) – $\mathbf{e}_\eta = \mathbf{e}_\zeta \times \mathbf{e}_\xi$.

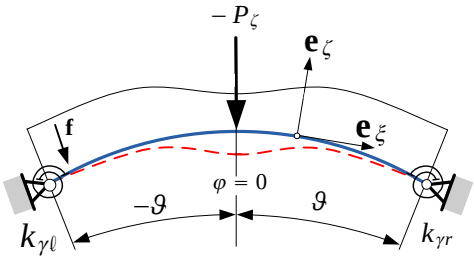

Figure 1. Rotationally restrained arch.

Under cross-sectional heterogeneity is meant that the material parameters – the Young's modulus E and the Poison's number ν – are functions of the cross-sectional coordinates η and ζ (that is, these are independent of ξ): $E(\eta,\zeta) = E(-\eta,\zeta)$, $\nu(\eta,\zeta) = \nu(-\eta,\zeta)$. Otherwise, the material of the arch is isotropic. The cross-section is uniform and symmetric with respect to the coordinate plane (ξ,ζ). The E-weighted centerline, along which the coordinates $\xi = s$ are measured, is assumed to remain in the coordinate plane (ξ,ζ). The position of the point at which the E-weighted centerline intersects the cross-section is obtained from the condition

$$Q_{e\eta} = \int_A E(\eta,\zeta)\,\zeta\,\mathrm{d}A = 0, \tag{1}$$

in which the integral is the E-weighted first moment with respect to the axis η – this quantity is denoted by $Q_{e\eta}$. We assume that the displacement vector at an arbitrary point of the cross-section prior to buckling has the form

$$\mathbf{u} = \mathbf{u}_o + \psi_{o\eta}\zeta\mathbf{e}_\xi = w_o\mathbf{e}_\zeta + (u_o + \psi_{o\eta}\zeta)\mathbf{e}_\xi\ , \tag{2}$$

where $\mathbf{u}_o$ is the displacement vector of the centerline and $\psi_{o\eta}$ is the rigid body rotation there – Euler-Bernoulli beam theory is considered. The rotation can be determined in terms of the displacements as

$$\psi_{o\eta} = -\frac{1}{2}\,(\mathbf{u}\times\nabla)|_{\zeta=0}\cdot\mathbf{e}_\eta = \frac{u_o}{\rho_o} - \frac{\mathrm{d}w_o}{\mathrm{d}s}\ ,\quad \nabla = \frac{\rho_o}{\rho_o+\zeta}\frac{\partial}{\partial s}\mathbf{e}_\xi + \frac{\partial}{\partial\eta}\mathbf{e}_\eta + \frac{\partial}{\partial\zeta}\mathbf{e}_\zeta\,. \tag{3}$$

Nonlinearities are taken into account by keeping some nonlinear terms in the Green-Lagrange strain tensor, that is

$$\boldsymbol{E} = \boldsymbol{E}^L + \boldsymbol{E}^N,\quad \boldsymbol{E}^L = \frac{1}{2}\,(\mathbf{u}\circ\nabla + \nabla\circ\mathbf{u})\ ,\quad \boldsymbol{E}^N = \frac{1}{2}\,(\nabla\circ\mathbf{u})\cdot(\mathbf{u}\circ\nabla) \simeq \frac{1}{2}\boldsymbol{\Psi}\cdot\boldsymbol{\Psi}^T\ . \tag{4}$$

Here $\boldsymbol{\Psi}$ is the tensor of small rotations and, for shallow arches, it is dominant compared to the other quadratic components [15]. Consequently

$$\varepsilon_\xi = \mathbf{e}_\xi\cdot\frac{1}{2}\,(\mathbf{u}\circ\nabla + \nabla\circ\mathbf{u})\cdot\mathbf{e}_\xi + \mathbf{e}_\xi\cdot\frac{1}{2}\left(\boldsymbol{\Psi}^T\cdot\boldsymbol{\Psi}\right)\cdot\mathbf{e}_\xi = \frac{\rho_o}{\rho_o+\zeta}\,(\varepsilon_{o\xi} + \zeta\kappa_o) + \frac{1}{2}\psi_{o\eta}^2 \tag{5}$$

is the axial strain at an arbitrary point, where

$$\varepsilon_{o\xi} = \frac{\mathrm{d}u_o}{\mathrm{d}s} + \frac{w_o}{\rho_o}\,, \qquad \kappa_o = \frac{\mathrm{d}\psi_{o\eta}}{\mathrm{d}s} = \frac{1}{\rho_o}\frac{\mathrm{d}u_o}{\mathrm{d}s} - \frac{\mathrm{d}^2 w_o}{\mathrm{d}s^2} \quad \text{and} \quad \varepsilon_m = \varepsilon_{o\xi} + \frac{1}{2}\psi_{o\eta}^2\,. \tag{6}$$

Here $\varepsilon_{o\xi}$ and ε_m are the linear and the nonlinear axial strain on the centerline, further κ_o is the curvature there.

It is assumed that σ_ξ is much greater than any other element of the second Piola-Kirchhoff stress tensor. Under this condition $\sigma_\xi = E\varepsilon_\xi$ is the constitutive equation. The E-weighted reduced area A_{eR}, the E-weighted reduced moment of inertia I_{eR} and the E-weighted reduced first moment Q_{eR} are defined as

$$A_{eR} = \int_A \frac{\rho_o}{\rho_o+\zeta} E(\eta,\zeta)\,\mathrm{d}A \simeq \int_A E(\eta,\zeta)\,\mathrm{d}A = A_e\,, \tag{7a}$$

$$I_{eR} = \int_A \frac{\rho_o}{\rho_o+\zeta} E(\eta,\zeta)\zeta^2\,\mathrm{d}A \simeq \int_A \zeta^2 E(\eta,\zeta)\mathrm{d}A = I_{e\eta}\,, \tag{7b}$$

$$Q_{eR} = \int_A \frac{\rho_o}{\rho_o+\zeta} E(\eta,\zeta)\zeta\,\mathrm{d}A \simeq \frac{1}{\rho_o}\int_A \zeta^2 E(\eta,\zeta)\,\mathrm{d}A = -\frac{I_{e\eta}}{\rho_o}. \tag{7c}$$

With the aid of these quantities and by recalling the kinematic relations (5)-(6), we get the axial force and the bending moment:

$$N = \int_A E\varepsilon_\xi\,\mathrm{d}A = A_{eR}\varepsilon_{o\xi} + Q_{eR}\kappa_o + A_e\frac{1}{2}\psi_{o\eta}^2 \approx A_e\varepsilon_m - \frac{I_{e\eta}}{\rho_o}\kappa_o\,, \tag{8}$$

$$M = \int_A E\varepsilon_\xi\zeta\,\mathrm{d}A = \underbrace{\int_A E\frac{\zeta}{1+\frac{\zeta}{\rho_o}}\,\mathrm{d}A}_{Q_{eR}\simeq -\frac{I_{e\eta}}{\rho_o}}\varepsilon_{o\xi} + \underbrace{\int_A E\frac{\zeta^2}{1+\frac{\zeta}{\rho_o}}\,\mathrm{d}A}_{I_{eR}\simeq I_{e\eta}}\kappa_o + \underbrace{\int_A E\zeta\,\mathrm{d}A}_{Q_{e\eta}=0}\frac{1}{2}\psi_{o\eta}^2 =$$

$$= -I_{e\eta}\left(\frac{\mathrm{d}^2 w_o}{\mathrm{d}s^2} + \frac{w_o}{\rho_o^2}\right)\,. \tag{9}$$

With the knowledge of the bending moment we can check – by utilizing (8) and $(6)_{2,3}$ – that

$$N = \frac{I_{e\eta}}{\rho_o^2}\left(\frac{A_e\rho_o^2}{I_{e\eta}} - 1\right)\varepsilon_m - \frac{M}{\rho_o} \approx A_e\varepsilon_m - \frac{M}{\rho_o}\,. \tag{10}$$

2.2. **Post-buckling state.** Quantities denoted by an asterisk belong to the post-buckling equilibrium state, while the change (increment) between the pre- and post-buckling equilibrium is denoted by a subscript $_b$. (The change from the initial configuration to the pre-buckling state is not denoted specifically.) Making use of this convention, similarly as before, we can derive the rotation field and the change of curvature as

$$\psi_{o\eta}^* = \psi_{o\eta} + \psi_{o\eta\,b}\,, \quad \psi_{o\eta\,b} = \frac{u_{ob}}{\rho_o} - \frac{\mathrm{d}w_{ob}}{\mathrm{d}s}\,, \quad \kappa_o^* = \kappa_o + \kappa_{o\,b}\,, \quad \kappa_{o\,b} = \frac{1}{\rho_o}\frac{\mathrm{d}u_{ob}}{\mathrm{d}s} - \frac{\mathrm{d}^2 w_{ob}}{\mathrm{d}s^2}\,. \tag{11}$$

As regards the strain increment (assuming $\left|\frac{1}{2}\psi_{o\eta\,b}^2\right| \ll |\psi_{o\eta}\psi_{o\eta\,b}|$, which is generally accepted in the literature) we have

$$\varepsilon_\xi^* = \frac{\rho_o}{\rho_o+\zeta}\left(\varepsilon_{o\xi}^* + \zeta\kappa_o^*\right) + \frac{1}{2}\left(\psi_{o\eta}^*\right)^2 = \varepsilon_\xi + \varepsilon_{\xi\,b},\quad \varepsilon_{\xi\,b} \simeq \frac{\rho_o}{\rho_o+\zeta}\left(\varepsilon_{o\xi\,b} + \zeta\kappa_{o\,b}\right) + \psi_{o\eta\,b}\psi_{o\,\eta}\,; \tag{12a}$$

$$\varepsilon_{o\xi\,b} = \frac{\mathrm{d}u_{ob}}{\mathrm{d}s} + \frac{w_{ob}}{\rho_o}\,,\quad \varepsilon_{mb} \simeq \varepsilon_{o\xi\,b} + \psi_{o\eta\,b}\psi_{o\,\eta}\,. \tag{12b}$$

Recalling (7), (8), (10) and (12) we can write

$$N^* = \int_A E\varepsilon_\xi^*\,\mathrm{d}A = N + N_b\,,\qquad N_b = A_e\varepsilon_{m\,b} - \frac{I_{e\eta}}{\rho_o}\kappa_{ob}\,. \tag{13}$$

In the same way we obtain the increment in the bending moment as

$$M^* = \int_A E\varepsilon_\xi^*\zeta\,\mathrm{d}A = M + M_b\,,\qquad M_b = -I_{e\eta}\left(\frac{\mathrm{d}^2 w_{ob}}{\mathrm{d}s^2} + \frac{w_{ob}}{\rho_o^2}\right). \tag{14}$$

Let us assume that

$$A_e\rho_o^2/I_{e\eta} - 1 \approx A_e\rho_o^2/I_{e\eta} = (\rho_o/i_e)^2 = m\,,\quad i_e = \sqrt{I_{e\eta}/A_e}\,. \tag{15}$$

Here i_e is the E-weighted radius of gyration and m is the slenderness ratio of the arch. The latter (heterogeneity) parameter is of particular importance as the computational results will significantly depend on it.

With the knowledge of the increment in the bending moment we can check, in the same way as we did for equation (10), that

$$N_b = \frac{I_{e\eta}}{\rho_o^2}\left(\frac{A_e\rho_o^2}{I_{e\eta}} - 1\right)\varepsilon_{mb} - \frac{M_b}{\rho_o} \approx A_e\varepsilon_{m\,b} - \frac{M_b}{\rho_o}\,. \tag{16}$$

It should be pointed out that Bradford et al. have assumed $\rho_o/(\rho_o+\zeta) = 1$ when expressing the axial strain and the strain increment at an arbitrary point. They have also neglected the terms M/ρ_o and M_b/ρ_o in their corresponding article when expressing the axial force and its increment – compare (10) and (16) with (15) and (47) in [17]

We shall change derivatives with respect to s to derivatives with respect to φ by using the following equation:

$$\frac{\mathrm{d}^n(\ldots)}{\mathrm{d}s^n} = \frac{1}{\rho_o^n}\frac{\mathrm{d}^n(\ldots)}{\mathrm{d}\varphi^n} = (\ldots)^{(n)}\,,\quad n \in \mathbb{Z}. \tag{17}$$

This transformation is carried out, where necessary without a remark.

3. Governing equations

3.1. **Equations of the pre-buckling equilibrium.** Assuming symmetric loading and support conditions Figure 1 shows the centerline in the initial configuration (continuous line) and in the pre-buckling equilibrium (dashed line). We shall assume in a more general approach that the arch with a central angle of 2ϑ is subjected to the concentrated force P_ζ at the crown as well as to the arbitrary distributed line load

$\mathbf{f} = f_t\mathbf{e}_\xi + f_n\mathbf{e}_\zeta$. Moreover, the [left] (right) end of the arch is rotationally restrained by torsional springs with spring stiffness $[k_{\gamma\ell}]$ $(k_{\gamma\, r})$. The principle of virtual work is given by

$$\int_V \sigma_\xi \delta\varepsilon_\xi \,\mathrm{d}V = -P_\zeta\ \delta w_o|_{s=0} - k_{\gamma\ell}\psi_{o\eta}\delta\psi_{o\eta}|_{s(-\vartheta)} - k_{\gamma r}\psi_{o\eta}\delta\psi_{o\eta}|_{s(\vartheta)} + \\ + \int_{\mathcal{L}} (f_n\delta w_o + f_t\delta u_o)\,\mathrm{d}s, \quad (18)$$

where the virtual quantities are preceded by the symbol δ. After substituting the kinematic equations (5) and (6) in terms of the virtual quantities and applying then formulae (8) and (9) established for the inner forces, the integration by parts theorem leads to a form of the principle of virtual work from which, with regard to the arbitrariness of the virtual quantities, we get the equilibrium equations

$$\begin{aligned} &\frac{\mathrm{d}N}{\mathrm{d}s} + \frac{1}{\rho_o}\left[\frac{\mathrm{d}M}{\mathrm{d}s} - \left(N + \frac{M}{\rho_o}\right)\psi_{o\eta}\right] + f_t = 0\,, \\ &\frac{\mathrm{d}}{\mathrm{d}s}\left[\frac{\mathrm{d}M}{\mathrm{d}s} - \left(N + \frac{M}{\rho_o}\right)\psi_{o\eta}\right] - \frac{N}{\rho_o} + f_n = 0\,. \end{aligned} \quad (19)$$

It also follows from the principle of virtual work that boundary conditions can be imposed on

$$N|_{s(\pm\vartheta)} \qquad \text{or} \qquad u_o|_{s(\pm\vartheta)}\ , \quad (20a)$$

$$\left[\frac{\mathrm{d}M}{\mathrm{d}s} - \left(N + \frac{M}{\rho_o}\right)\psi_{o\eta}\right]\Big|_{s(\pm\vartheta)} \qquad \text{or} \qquad w_o|_{s(\pm\vartheta)}\ , \quad (20b)$$

$$(M \pm k_\gamma\psi_{o\eta})|_{s(\pm\vartheta)} \qquad \text{or} \qquad \psi_{o\eta}|_{s(\pm\vartheta)}\,, \quad (20c)$$

where it is assumed that $k_{\gamma\ell} = k_{\gamma\, r} = k_\gamma$. In addition, the discontinuity condition

$$\left[\frac{\mathrm{d}M}{\mathrm{d}s} - \left(N + \frac{M}{\rho_o}\right)\psi_{o\eta}\right]\Big|_{s=+0} - \left[\frac{\mathrm{d}M}{\mathrm{d}s} - \left(N + \frac{M}{\rho_o}\right)\psi_{o\eta}\right]\Big|_{s=-0} - P_\zeta = 0 \quad (21)$$

for the shear force at the crown point should also be fulfilled.

In the sequel we assume $f_t = f_n = 0$. Upon substitution of equation (6) into equation $(19)_1$ we get

$$\frac{\mathrm{d}}{\mathrm{d}s}\left(A_e\varepsilon_m\right) - \frac{1}{\rho_o}\left(A_e\varepsilon_m\psi_{o\eta}\right) = 0\,. \quad (22)$$

Let us now neglect the quadratic term $\varepsilon_m\psi_{o\eta}$. Consequently, we arrive at

$$\frac{\mathrm{d}\varepsilon_m}{\mathrm{d}s} \simeq \frac{\mathrm{d}\varepsilon_{o\xi}}{\mathrm{d}s} = 0 \quad \rightarrow \quad \varepsilon_m \simeq \varepsilon_{o\xi} = \text{constant}, \quad (23)$$

which shows, depending on which theory is applied, that the nonlinear/linear strain on the centerline is constant.

If we introduce (3) and $(6)_{1,3}$ into the expression $\rho_o\varepsilon_m\left(1 + \psi_{o\eta}^{(1)}\right)$ we arrive at the following result (the quadratic term is neglected when that is compared to the others):

$$\rho_o\varepsilon_m\left(1+\psi_{o\eta}^{(1)}\right)=\rho_o\varepsilon_m\left[1+\frac{1}{\rho_o}\left(u_o^{(1)}-w_o^{(2)}\right)\right]=$$
$$=\rho_o\varepsilon_m\left[1+\frac{1}{\rho_o}\left(\rho_o\varepsilon_m-w_o-\frac{1}{2}\psi_{o\eta}^2\rho_o-w_o^{(2)}\right)\right]\approx$$
$$\approx\rho_o\varepsilon_m\underbrace{(1+\varepsilon_m)}_{\approx 1}-\varepsilon_m\left(w_o+w_o^{(2)}\right)\approx\rho_o\varepsilon_m-\varepsilon_m\left(w_o^{(2)}+w_o\right)\,. \quad (24)$$

Substitute now formulae (9) and (10) into $(19)_2$ and take equations (23) and (24) into account. After some manipulations we have

$$W_o^{(4)}+\left(\chi^2+1\right)W_o^{(2)}+\chi^2 W_o=\chi^2-1\,,\qquad \chi^2=1-m\varepsilon_m\,. \quad (25)$$

Here and in the sequel $W_o=w_o/\rho_o$ and $U_o=u_o/\rho_o$ are dimensionless displacements. Equation (25) can be compared with the equation Bradford et al. have used in their series of articles published recently on stability problems of shallow arches. This equation is of the form

$$W_o^{(4)}+(\chi^2-1)W_o^{(2)}=\chi^2-1. \quad (26)$$

Equation (25) includes less neglects than that derived by Bradford et al. – see, e.g., [15], [17].

3.2. **Equations of the post-buckling equilibrium.** The principle of virtual work for the buckled equilibrium configuration assumes the form

$$\int_V \sigma_\xi^*\delta\varepsilon_\xi^*\,\mathrm{d}V=-P_\zeta^*\;\delta w_o^*\big|_{s=0}-k_{\gamma\ell}\psi_{o\eta}^*\delta\psi_{o\eta}^*\big|_{s(-\vartheta)}-k_{\gamma r}\psi_{o\eta}^*\delta\psi_{o\eta}^*\big|_{s(\vartheta)}+$$
$$+\int_{\mathcal{L}}\left(f_n^*\delta w_o^*+f_t^*\delta u_o^*\right)\,\mathrm{d}s\,. \quad (27)$$

By repeating the line of thought leading to (19),(20) and taking into account that (a) the principle of virtual work should be fulfilled in the pre-buckling state; (b) $P_{\zeta b}=0$ and $k_{\gamma\ell}=k_{\gamma\,r}=k_\gamma$ the principle of virtual work yields

$$\frac{\mathrm{d}N_b}{\mathrm{d}s}+\frac{1}{\rho_o}\frac{\mathrm{d}M_b}{\mathrm{d}s}-\frac{1}{\rho_o}\left(N+\frac{M}{\rho_o}\right)\psi_{o\eta\,b}-\frac{1}{\rho_o}\left(N_b+\frac{M_b}{\rho_o}\right)\psi_{o\eta\,b}+f_{tb}=0\,, \quad (28a)$$

$$\frac{\mathrm{d}^2M_b}{\mathrm{d}s^2}-\frac{N_b}{\rho_o}-\frac{\mathrm{d}}{\mathrm{d}s}\left[\left(N+N_b+\frac{M+M_b}{\rho_o}\right)\psi_{o\eta\,b}+\left(N_b+\frac{M_b}{\rho_o}\right)\psi_{o\eta}\right]+f_{nb}=0, \quad (28b)$$

which govern the post-buckling equilibrium. For the buckled configuration, boundary conditions can be prescribed on the following quantities:

$$N_b\big|_{s(\pm\vartheta)}\quad\text{or}\quad u_{ob}\big|_{s(\pm\vartheta)}\,, \quad (29a)$$

$$\left[\frac{\mathrm{d}M_b}{\mathrm{d}s}-\left(N+N_b+\frac{M+M_b}{\rho_o}\right)\psi_{o\eta\,b}-\left(N_b+\frac{M_b}{\rho_o}\right)\psi_{o\eta}\right]\Big|_{s(\pm\vartheta)}\quad\text{or}\quad w_{ob}\big|_{s(\pm\vartheta)}\,, \quad (29b)$$

$$(M_b \pm k_\gamma \psi_{o\eta})|_{s(\pm\vartheta)} \quad \text{or} \quad \psi_{o\eta\, b}|_{s(\pm\vartheta)} \ . \tag{29c}$$

In the forthcoming it is assumed that $f_{tb} = f_{nb} = 0$. Observe that, apart from the last but one term, (28a) formally coincides with $(19)_1$. However, since the term mentioned is quadratic in the increment, it can be neglected with a good accuracy. Therefore repeating now a similar line of thought leading to (23), we obtain that the strain increment is constant:

$$\frac{\mathrm{d}}{\mathrm{d}s}\left(A_e \varepsilon_{mb}\right) - \underbrace{\frac{1}{\rho_o}\left(A_e \varepsilon_m \psi_{o\eta b}\right)}_{\text{it can also be neglected}} = 0 \quad \Rightarrow \quad \varepsilon_{m\,b} \simeq \varepsilon_{o\xi\,b} = \text{constant} \ . \tag{30}$$

If we (a) take into account that $\varepsilon_m^{(1)} = \varepsilon_{mb}^{(1)} = 0$; (b) substitute M_b from (14) and (c) utilize that

$$m\rho_o\varepsilon_{mb}\left(1+\psi_{o\eta}^{(1)}\right) \simeq m\rho_o\varepsilon_{mb}\left[1-\frac{1}{\rho_o}\left(w_o^{(2)}+w_o\right)\right] = m\rho_o\varepsilon_{mb} - m\varepsilon_{mb}\left(w_o^{(2)}+w_o\right)$$

(this relation can be set up in the same way as (24)) then, after some manipulations, (28b) results in

$$W_{ob}^{(4)} + (\chi^2+1)W_{ob}^{(2)} + \chi^2 W_{ob} = m\varepsilon_{mb}\left[1-\left(W_o^{(2)}+W_o\right)\right] \ . \tag{31}$$

This equation is again comparable with the outcome derived by Bradford et al. – e.g., [15], [17] – that is

$$W_{ob}^{(4)} + (\chi^2-1)W_{ob}^{(2)} = m\varepsilon_{mb}\left[1-W_o^{(2)}\right] \ . \tag{32}$$

4. Solution for the pre-buckling state

The general solution satisfying (25) for the dimensionless normal displacement is of the form

$$W_o(\varphi) = \frac{\chi^2-1}{\chi^2} + A_1\cos\varphi + A_2\sin\varphi - \frac{A_3}{\chi^2}\cos\chi\varphi - \frac{A_4}{\chi^2}\sin\chi\varphi, \tag{33}$$

in which A_i $(i=1,\ldots,4)$ are integration constants. Since all the geometry, the loading and the supports are symmetric, it is sufficient to consider a half of the arch as the pre-buckling shape is also symmetric. To determine the integration constants, we shall use the boundary conditions (BCs) presented in Table 1 – $\mathcal{P} = -P_\zeta \rho_o^2 \vartheta / 2I_{e\eta}$ is the dimensionless load and $\mathcal{S} = \rho_o k_\gamma / I_{e\eta}$ is the dimensionless stiffness of the restraints.

Table 1. Boundary conditions for the rotationally restrained arch.

Boundary conditions	
Crown point	Right end
$\psi_{o\eta}\big\|_{\varphi=+0} = 0 \rightarrow W_o^{(1)}\Big\|_{\varphi=+0} = 0$	$W_o\big\|_{\varphi=\vartheta} = 0$
$\left[-\frac{\mathrm{d}M}{\mathrm{d}s}+\frac{P_\zeta}{2}\right]_{\varphi=+0} = 0 \rightarrow W_o^{(3)}\Big\|_{\varphi=+0} = \frac{\mathcal{P}}{\vartheta}$	$[M + k_\gamma \psi_{o\,\eta}]\big\|_{\varphi=\vartheta} = 0 \rightarrow \left[W_o^{(2)} + \mathcal{S}W_o^{(1)}\right]\Big\|_{\varphi=\vartheta} = 0$

For the sake of brevity let us introduce the constant

$$a = \left(\chi^2 - 1\right)\cos\vartheta\cos\chi\vartheta - \mathcal{S}\left(\sin\vartheta\cos\chi\vartheta - \chi\cos\vartheta\sin\chi\vartheta\right) . \tag{34}$$

Solution (33) satisfies the boundary conditions if

$$A_1 = A_{11} + \frac{\mathcal{P}}{\vartheta}A_{12} = \frac{\left(1-\chi^2\right)\left(\chi\cos\chi\vartheta + \mathcal{S}\sin\chi\vartheta\right)}{\chi a} + \\ + \frac{\left(1-\chi^2\right)\sin\vartheta\cos\chi\vartheta - \mathcal{S}\left(\cos\vartheta\cos\chi\vartheta + \chi\sin\vartheta\sin\chi\vartheta - 1\right)}{\left(\chi^2-1\right)a}\frac{\mathcal{P}}{\vartheta}, \tag{35a}$$

$$A_2 = \frac{1}{\left(\chi^2-1\right)}\frac{\mathcal{P}}{\vartheta} = A_{22}\frac{\mathcal{P}}{\vartheta}; \tag{35b}$$

$$A_3 = A_{31} + \frac{\mathcal{P}}{\vartheta}A_{32} = \frac{\cos\vartheta + \mathcal{S}\sin\vartheta}{-a} + \\ + \frac{\chi\left[\left(\chi^2-1\right)\cos\vartheta\sin\chi\vartheta - \mathcal{S}\left(\sin\vartheta\sin\chi\vartheta + \chi\cos\vartheta\cos\chi\vartheta - \chi\right)\right]}{-\left(\chi^2-1\right)a}\frac{\mathcal{P}}{\vartheta} , \tag{35c}$$

$$A_4 = \frac{\chi}{\left(\chi^2-1\right)}\frac{\mathcal{P}}{\vartheta} = A_{42}\frac{\mathcal{P}}{\vartheta} . \tag{35d}$$

If $[\mathcal{S} = 0]$ $(\mathcal{S} \to \infty)$ we get back the results valid for [pinned-pinned] (fixed-fixed) arches – see [20], [21]. The radial displacement for the whole arch is given by

$$W_o = \frac{\chi^2-1}{\chi^2} + A_{11}\cos\varphi - \frac{A_{31}}{\chi^2}\cos\chi\varphi + \\ + \left(A_{12}\cos\varphi + A_{22}H\sin\varphi - \frac{A_{32}}{\chi^2}\cos\chi\varphi - \frac{A_{42}}{\chi^2}H\sin\chi\varphi\right)\frac{\mathcal{P}}{\vartheta}; \tag{36}$$

in which $H = H(\varphi) = 1$ if $\varphi > 0$ and $H = H(\varphi) = -1$ if $\varphi < 0$. The rotation field (by neglecting the effects of the tangential displacement due to the shallowness) is

$$\psi_{o\eta} \simeq -W_o^{(1)} = B_{11}\sin\varphi + B_{31}\sin\chi\varphi + \\ + \left(B_{12}\sin\varphi + B_{22}H\cos\varphi + B_{32}\sin\chi\varphi + B_{42}H\cos\chi\varphi\right)\frac{\mathcal{P}}{\vartheta}; \tag{37}$$

where the new constants are

$$B_{11} = A_{11} , \quad B_{12} = A_{12} , \quad B_{22} = -A_{22} , \quad B_{31} = -\frac{A_{31}}{\chi} , \quad B_{32} = -\frac{A_{32}}{\chi} , \quad B_{42} = \frac{A_{42}}{\chi} .$$

Because the strain on the centerline is constant, based on (23), the mathematical average of the strain, i.e., the strain itself, is given by

$$\varepsilon_m = \frac{1}{\vartheta}\int_0^{\vartheta}\varepsilon_m \mathrm{d}\varphi = \frac{1}{\vartheta}\int_0^{\vartheta}\left(\varepsilon_{o\xi} + \frac{1}{2}\psi_{o\eta}^2\right)\mathrm{d}\varphi = \frac{1}{\vartheta}\int_0^{\vartheta}\left(U_o^{(1)} + W_o + \frac{1}{2}\psi_{o\eta}^2\right)\mathrm{d}\varphi; \tag{38}$$

where

$$\frac{1}{\vartheta}\int_0^{\vartheta} U_o^{(1)}\mathrm{d}\varphi = U_o|_0^{\vartheta} = 0. \tag{39}$$

Equation (38) results in the

$$I_2\mathcal{P}^2 + I_1\mathcal{P} + I_0 - \varepsilon_m = 0\,, \qquad I_j(m,\vartheta,\chi,\mathcal{S}) \in \mathbb{R}, \quad j = 0,1,2 \tag{40}$$

quadratic formula for the dimensionless force, in which the coefficients I_j can be obtained in a closed form – see Appendix A.1 for details.

5. Solutions for the post-buckling state

5.1. **Differential equations, which govern the problem.** Substitution of the solution (36) into the post-buckling equilibrium equation (31) yields

$$W_{ob}^{(4)} + (1+\chi^2)W_{ob}^{(2)} + \chi^2 W_{ob} = -m\varepsilon_{mb}\frac{1-\chi^2}{\chi^2}\left(\frac{1}{1-\chi^2} + A_3\cos\chi\varphi + A_4\sin\chi\varphi\right). \tag{41}$$

In general, there are two possibilities regarding the buckled equilibrium of the arch [15]. When the strain increment ε_{mb} is constant but not equal to zero, the problem is governed by the above relation and the buckled shape is symmetric. However, it is also possible that the arch buckles antisymmetrically with no strain increment ($\varepsilon_{mb} = 0$). Then the phenomenon is described by the

$$W_{ob}^{(4)} + (1+\chi^2)W_{ob}^{(2)} + \chi^2 W_{ob} = 0 \tag{42}$$

homogeneous differential equation. The mathematical average of the strain increment, that is, the strain increment itself can be determined by using the kinematical equations (3), (10) and (12b) under the assumption that the effect of the normal displacement is again negligible when calculating the rotation increment:

$$\varepsilon_{mb} \simeq \frac{1}{2\vartheta}\int_{-\vartheta}^{\vartheta}(\varepsilon_{o\xi\,b}+\psi_{o\eta\,b}\psi_{o\eta})\,\mathrm{d}\varphi = \frac{1}{2\vartheta}\int_{-\vartheta}^{\vartheta}\left[U_{ob}^{(1)}+W_{ob}+\left(U_{ob}-W_{ob}^{(1)}\right)\left(U_o-W_o^{(1)}\right)\right]\mathrm{d}\varphi \approx$$
$$\approx \frac{1}{2\vartheta}\int_{-\vartheta}^{\vartheta}\left(W_{ob}+W_{ob}^{(1)}W_o^{(1)}\right)\mathrm{d}\varphi. \tag{43}$$

It will later be shown that antisymmetric shape belongs to bifurcation buckling, while in the case of a snap-through (or limit point) buckling the shape of the arch is always symmetric.

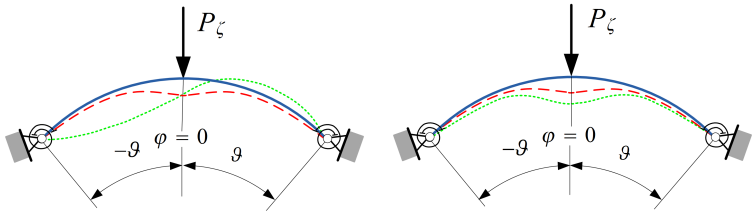

Figure 2. Antisymmetric and symmetric buckling shapes.

In Figure 2 the continuous lines show the centerline in the initial configuration, the dashed lines represent the pre-buckling equilibrium state and the dotted lines illustrate the buckled arch shapes for antisymmetric and symmetric buckling.

5.2. **Antisymmetric buckling.** The solution to the homogeneous equilibrium equation (42) is sought for the whole arch as

$$W_{ob}(\varphi) = C_1 \cos\varphi + C_2 \sin\varphi + C_3 \sin\chi\varphi + C_4 \cos\chi\varphi\,, \tag{44}$$

where C_i $(i = 1, \ldots, 4)$ are integration constants. It is paired with the homogeneous BCs gathered in Table 2.

Table 2. Boundary conditions in terms of W_{ob}.

Boundary conditions	
Left end	Right end
$W_{ob}\big\vert_{\varphi=-\vartheta} = 0$	$W_{ob}\big\vert_{\varphi=\vartheta} = 0$
$\left(-W_{ob}^{(2)} + \mathcal{S}W_{ob}^{(1)}\right)\Big\vert_{\varphi=-\vartheta} = 0$	$\left(W_{ob}^{(2)} + \mathcal{S}W_{ob}^{(1)}\right)\Big\vert_{\varphi=\vartheta} = 0$

Upon substitution of solution (44) into the boundary conditions, we arrive at a homogeneous equation system for which solution different from the trivial one exists if the determinant of the coefficient matrix vanishes:

$$\begin{aligned}\mathcal{D} = &\left[\left(\chi^2-1\right)\sin\vartheta\sin\chi\vartheta + \mathcal{S}\left(\cos\vartheta\sin\chi\vartheta - \chi\sin\vartheta\cos\chi\vartheta\right)\right]\times\\ &\times\left[\left(\chi^2-1\right)\cos\vartheta\cos\chi\vartheta + \mathcal{S}\left(\chi\cos\vartheta\sin\chi\vartheta - \sin\vartheta\cos\chi\vartheta\right)\right] = 0\,.\end{aligned} \tag{45}$$

Vanishing of the first factor in (45) results in the transcendental equation

$$\frac{\mathcal{S}\chi\tan\vartheta}{\mathcal{S} + (\chi^2-1)\tan\vartheta} = \tan\chi\vartheta. \tag{46}$$

Some numerical solutions for $\mathfrak{F} = \chi\vartheta$ in terms of the ϑ are plotted in Figure 3. When $[\mathcal{S} = 0](\mathcal{S} \to \infty)$ this characteristic equation coincides with that valid for [pinned-pinned](fixed-fixed) arches – see [20], [21].

Recalling $(25)_2$, we get the critical strain for antisymmetric buckling:

$$\varepsilon_{m\,cr\,anti} = \frac{1-\chi^2}{m} = \frac{1}{m}\left[1 - \left(\frac{\mathfrak{F}(\vartheta,\mathcal{S})}{\vartheta}\right)^2\right]. \tag{47}$$

If we now substitute the solution (46) back to the boundary conditions, it follows that $C_1 = C_4 = 0$ and $C_2 = -C_3\sin\chi\vartheta/\sin\vartheta$. Consequently, recalling the general solution (44), we get that the shape of the arch is antisymmetric:

$$W_{ob}(\varphi) = C_3\left(\sin\chi\varphi - \frac{\sin\chi\vartheta}{\sin\vartheta}\sin\varphi\right) = C_3\left(\sin\frac{\mathfrak{F}}{\vartheta}\varphi - \frac{\sin\mathfrak{F}}{\sin\vartheta}\sin\varphi\right). \tag{48}$$

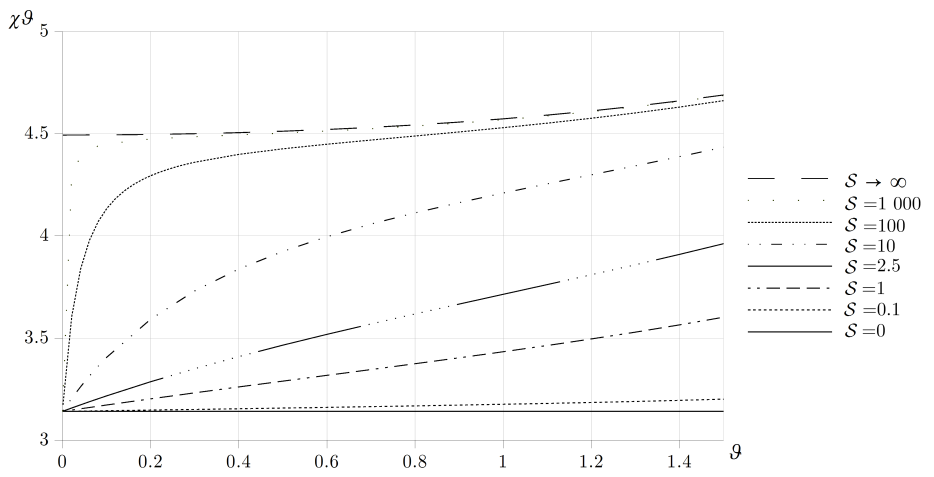

Figure 3. Some solutions to $\mathfrak{F}(\vartheta, \mathcal{S})$.

Vanishing of the second factor in (45) yields

$$\left(\chi^2 - 1\right) + \mathcal{S}\left(\chi \tan \chi\vartheta - \tan \vartheta\right) = 0\,. \tag{49}$$

After solving the above equation for $\mathfrak{G} = \chi\vartheta$, we find that a symmetric buckling shape is the solution for the radial displacement with $C_2 = C_3 = 0$ and $C_1 = C_4 \cos \chi\vartheta / \cos \vartheta$:

$$W_{ob}(\varphi) = C_4 \left(\cos \chi\varphi - \frac{\cos \chi\vartheta}{\cos \vartheta} \cos \varphi\right) = C_4 \left(\cos \frac{\mathfrak{G}}{\vartheta}\varphi - \frac{\cos \mathfrak{G}}{\cos \vartheta} \cos \varphi\right)\,. \tag{50}$$

5.3. **Symmetric snap-through buckling.** The general solution to the inhomogeneous equation (41) is

$$W_{ob}(\varphi) = D_1 \cos \varphi + D_2 \sin \varphi + D_3 \sin \chi\varphi + D_4 \cos \chi\varphi - \\ - \frac{m\varepsilon_{m\,b}}{2\chi^3} \left(\frac{2}{\chi} + A_3 \varphi \sin \chi\varphi - A_4 \varphi \cos \chi\varphi\right)\,. \tag{51}$$

Since now the buckled shape is symmetric, the BCs collected in Table 3 are valid for the right half-arch.

Table 3. Boundary conditions for symmetric buckling.

Boundary conditions	
Crown point	Right end
$W_{ob}^{(1)}\Big\vert_{\varphi=0} = 0$	$W_{ob}\vert_{\varphi=\vartheta} = 0$
$W_{ob}^{(3)}\Big\vert_{\varphi=0} = 0$	$W_{ob}^{(2)} + \mathcal{S} W_{ob}^{(1)}\Big\vert_{\varphi=\vartheta} = 0$

Upon substitution of solution (51) into the boundary conditions, we get a system of linear equations from which

$$
\begin{aligned}
D_1 &= \varepsilon_{mb}\left(\hat{D}_{11}+\hat{D}_{12}\frac{\mathcal{P}}{\vartheta}\right)= \\
&= \varepsilon_{mb}\frac{m}{\chi^3 a}\left\{A_{31}\left[\chi\cos^2\chi\vartheta+0.5\mathcal{S}\left(\vartheta\chi+\cos\chi\vartheta\sin\chi\vartheta\right)\right]+\left(\chi\cos\chi\vartheta+\mathcal{S}\sin\chi\vartheta\right)\right\}+ \\
&\quad+\varepsilon_{mb}\frac{m}{2\chi^3\left(1-\chi^2\right)a}\Bigg\{A_{32}\left(1-\chi^2\right)\left[2\chi\cos^2\chi\vartheta+\mathcal{S}\left(\vartheta\chi+\cos\chi\vartheta\sin\chi\vartheta\right)\right]+ \\
&\qquad+A_{42}\left[2\chi\left(1-\chi^2\right)\left(\sin\chi\vartheta-\chi\sin\vartheta\right)\cos\chi\vartheta+\right. \\
&\left.+\mathcal{S}\left(2\chi^2\cos\vartheta\cos\chi\vartheta+2\chi^3\sin\vartheta\sin\chi\vartheta-3\chi^2+1+\left(\chi^2-1\right)\cos^2\chi\vartheta\right)\right]\Bigg\}\frac{\mathcal{P}}{\vartheta}\,, \qquad (52a)
\end{aligned}
$$

$$
D_2=\varepsilon_{mb}\hat{D}_{22}\frac{\mathcal{P}}{\vartheta}=\varepsilon_{mb}\frac{mA_{42}}{\left(\chi^2-1\right)\chi}\frac{\mathcal{P}}{\vartheta}\,,\quad D_3=\varepsilon_{mb}\hat{D}_{32}\frac{\mathcal{P}}{\vartheta}=\varepsilon_{mb}\frac{A_{42}m\left(3\chi^2-1\right)}{2\chi^4\left(1-\chi^2\right)}\frac{\mathcal{P}}{\vartheta}\,, \qquad (52b)
$$

$$
\begin{aligned}
D_4 &= \varepsilon_{mb}\left(\hat{D}_{41}+\hat{D}_{42}\frac{\mathcal{P}}{\vartheta}\right)= \\
&\quad=\varepsilon_{mb}\frac{m\cos\vartheta}{-2\chi^4 a}\Bigg\{2\left(1+\mathcal{S}\tan\vartheta\right)+A_{31}\chi\left[2\chi-\vartheta\left(\chi^2-1\right)\tan\chi\vartheta+\right. \\
&\qquad\left.+\mathcal{S}\left(\vartheta\tan\vartheta\tan\chi\vartheta+\tan\chi\vartheta+\chi\vartheta\right)\right]\cos\chi\vartheta\Bigg\}+ \\
&\quad+\varepsilon_{mb}\frac{m}{2\chi^4\left(\chi^2-1\right)a}\Bigg\{A_{32}\chi\left(1-\chi^2\right)\left[\left(2\chi-\vartheta\left(\chi^2-1\right)\tan\chi\vartheta\right)+\right. \\
&\qquad\left.+\mathcal{S}\left(\vartheta\tan\vartheta\tan\chi\vartheta+\tan\chi\vartheta+\chi\vartheta\right)\right]\cos\vartheta\cos\chi\vartheta+ \\
&\quad+A_{42}\Big[\left(1-\chi^2\right)^2\left(\tan\chi\vartheta-\chi\vartheta\right)\cos\vartheta\cos\chi\vartheta+\mathcal{S}\left[2\chi^3\left(1-\cos\vartheta\cos\chi\vartheta\right)+\right. \\
&\left.+\left(1-\chi^2\right)\vartheta\chi\left(\chi\tan\chi\vartheta-\tan\vartheta\right)\cos\vartheta\cos\chi\vartheta+\left(1-3\chi^2\right)\sin\vartheta\sin\chi\vartheta\right]\Big]\Bigg\}\frac{\mathcal{P}}{\vartheta} \qquad (52c)
\end{aligned}
$$

are the integration constants $D_i\,(i=1,\ldots,4)$. We remark that the constants $\hat{D}_{11}$, $\hat{D}_{12}$, $\hat{D}_{22}$, $\hat{D}_{32}$, $\hat{D}_{41}$ and $\hat{D}_{42}$ can be read off equations (52).

For the sake of brevity, we manipulate the particular solution to (51) into the following form:

$$
\begin{aligned}
W_{ob\,\mathrm{part}} &= -\varepsilon_{mb}\frac{m}{2\chi^3}\left[\frac{2}{\chi}+\left(A_{31}+A_{32}\frac{\mathcal{P}}{\vartheta}\right)\varphi\sin\chi\varphi-A_{42}\varphi\cos\chi\varphi\frac{\mathcal{P}}{\vartheta}\right]= \\
&\quad=\varepsilon_{mb}\left[-\frac{m}{\chi^4}-\frac{A_{31}m}{2\chi^3}\varphi\sin\chi\varphi+\left(-\frac{A_{32}m}{2\chi^3}\varphi\sin\chi\varphi+\frac{A_{42}m}{2\chi^3}\varphi\cos\chi\varphi\right)\frac{\mathcal{P}}{\vartheta}\right]= \\
&\qquad=\varepsilon_{mb}\left[\hat{D}_{01}+\hat{D}_{51}\varphi\sin\chi\varphi+\left(\hat{D}_{52}\varphi\sin\chi\varphi+\hat{D}_{62}\varphi\cos\chi\varphi\right)\frac{\mathcal{P}}{\vartheta}\right], \qquad (53a)
\end{aligned}
$$

where

$$\hat{D}_{01} = -\frac{m}{\chi^4}\,, \qquad \hat{D}_{51} = -\frac{A_{31}m}{2\chi^3}\,, \qquad \hat{D}_{52} = -\frac{A_{32}m}{2\chi^3}\,, \qquad \hat{D}_{62} = \frac{A_{42}m}{2\chi^3}\,. \tag{53b}$$

With the knowledge of the integration constants

$$W_{ob}(\varphi) = \varepsilon_{mb}\Big[\hat{D}_{01} + \hat{D}_{11}\cos\varphi + \hat{D}_{41}\cos\chi\varphi + \hat{D}_{51}\varphi\sin\chi\varphi + \\ + \Big(\hat{D}_{12}\cos\varphi + \hat{D}_{22}H\sin\varphi + \hat{D}_{32}H\sin\chi\varphi + \hat{D}_{42}\cos\chi\varphi + \\ + \hat{D}_{52}\varphi\sin\chi\varphi + \hat{D}_{62}H\varphi\cos\chi\varphi\Big)\frac{\mathcal{P}}{\vartheta}\Big] \tag{54}$$

is the solution for the complete arch. The increment in the rotation field for shallow arches is given by

$$-\psi_{o\eta\,b} \simeq W^{(1)}_{ob} = \varepsilon_{mb}\Big[E_{11}\sin\varphi + E_{41}\sin\chi\varphi + E_{51}\varphi\cos\chi\varphi + \\ + (E_{12}\sin\varphi + E_{22}\cos\varphi + E_{32}\cos\chi\varphi + E_{42}\sin\chi\varphi + \\ E_{52}\varphi\cos\chi\varphi + E_{62}\varphi\sin\chi\varphi)\frac{\mathcal{P}}{\vartheta}\Big]\,, \tag{55}$$

where

$$E_{11} = -\hat{D}_{11}\,, \quad E_{41} = \hat{D}_{51} - \hat{D}_{41}\chi\,, \quad E_{51} = \hat{D}_{51}\chi\,, \quad E_{12} = -\hat{D}_{12}\,, \quad E_{22} = \hat{D}_{22}H\,, \\ E_{32} = \hat{D}_{32}H\chi + \hat{D}_{62}H\,, \quad E_{42} = \hat{D}_{52} - \hat{D}_{42}\chi\,, \quad E_{52} = \hat{D}_{52}\,, \quad E_{62} = -\hat{D}_{62}H\,. \tag{56}$$

We can now calculate the mathematical average of the strain increment for the right half arch on the basis of (43). We get

$$1 = \frac{1}{\vartheta\varepsilon_{mb}}\int_0^{\vartheta}\Big(U^{(1)}_{ob} + W_{ob} + W^{(1)}_{o}W^{(1)}_{ob}\Big)\,\mathrm{d}\varphi = J_2\mathcal{P}^2 + J_1\mathcal{P} + J_0, \tag{57}$$

where the right side is also independent of ε_{mb}. Formulae for the coefficients (integrals) J_0, J_1 and J_2 are presented in Appendix A.1. Though the corresponding integrals can be given in a closed form, these are very long and are therefore omitted.

6. Computational results

6.1. **What to compute?** In this section results are presented for four different magnitudes of the parameter m. At first, we investigate how the spring stiffness affects the endpoints of the typical buckling intervals. Then the critical loads are calculated. The results are comparable with those obtained by Bradford et al. in [15] and [17] using more neglects but, due to this fact, arriving at analytical solutions. When $\mathcal{S} = 0$ and $\mathcal{S} \to \infty$ our results – since they are based on a similar mechanical model – coincide with those valid both for pinned-pinned [20] and for fixed-fixed [21] arches.

6.2. **Limits for the characteristic buckling intervals.** There are four intervals of interest regarding the buckling behavior of symmetrically supported shallow arches. For a given ϑ, the endpoints of these intervals are functions of m, $\chi(\varepsilon_m)$ and $\mathcal{S}$. The lower limit of antisymmetric buckling can be obtained from the condition that the discriminant of (40) should be real when the antisymmetric critical strain (46) is substituted, consequently inequality

$$\left[I_1^2 - 4I_2(I_0 - \varepsilon_{m\,cr\,anti})\right]\Big|_{\chi\vartheta=\mathfrak{F}} \geq 0 \tag{58}$$

should be fulfilled. We remark that when the spring stiffness is zero – i.e. the arch is pinned-pinned – instead of using the exact solution we assumed that $\mathfrak{F} = \pi - 10^{-4}$. It is also possible in certain cases that a real antisymmetric solution vanishes, so there is an upper limit also in the investigated $\vartheta = 0 \ldots 1.5$ range. The upper limit is obtained by using an algorithm which monitors at what value of $\mathcal{S}$ there exists no real solution any longer if $\chi\vartheta = \mathfrak{F}$.

When evaluating the critical antisymmetric and symmetric buckling loads against the geometry of the arch, we find that these two curves sometimes intersect each other. This intersection point varies with $\mathcal{S}$. There is a switch between the symmetric and antisymmetric buckling modes at the intersection point as it is shown in Section 6.4. Prior to the intersection, the symmetric buckling shape governs. However, after this intersection, the bifurcation point is located before the limit point of the corresponding primary equilibrium path, which means that antisymmetric buckling occurs first. (To better understand the meaning of limit point see Figure 12). This switch can be found when (40) and (57) are equal at $\chi\vartheta = \mathfrak{F}$ with all the other parameters being the same:

$$\left[I_2\mathcal{P}^2 + I_1\mathcal{P} + I_0 - \varepsilon_m\right]\Big|_{\mathfrak{F},m,\mathcal{S},\mathcal{P}} = \left[J_2\mathcal{P}^2 + J_1\mathcal{P} + J_0\right]\Big|_{\mathfrak{F},m,\mathcal{S},\mathcal{P}}. \tag{59}$$

Finally, the lower endpoint for symmetric buckling, below which there is no buckling at all, is obtained by substituting the lowest symmetric solution (49) into the pre-buckling averaged strain (40) when the discriminant is set to zero:

$$\left[I_1^2 - 4I_2(I_0 - \varepsilon_{m\,cr\,sym})\right]\Big|_{\chi\vartheta=\mathfrak{G}} = 0. \tag{60}$$

Now we turn the attention to the evaluation. Choosing $m = 1\,000$, Figure 4 shows the effects of the dimensionless spring stiffness in terms of the semi-vertex angle. When $\mathcal{S} = 0$, we get back the results valid for a pinned-pinned arch. Thus, when $\vartheta \leq 0.347$ there is no buckling – see the range denoted by (I). Then, up until $\vartheta = 0.5$, only symmetric limit point buckling can occur at the right loading level (II). Even though a bifurcation point (and therefore the possibility of antisymmetric buckling) appears when further increasing ϑ (III), still the symmetric shape is the dominant up until the intersection point of the symmetric and antisymmetric buckling curves at $\vartheta = 0.553$. At this point the buckling loads and strains are the same for symmetric and antisymmetric buckling and it holds a switch between the buckling types since above it (IV) the bifurcation point is located on the stabile branch of the primary

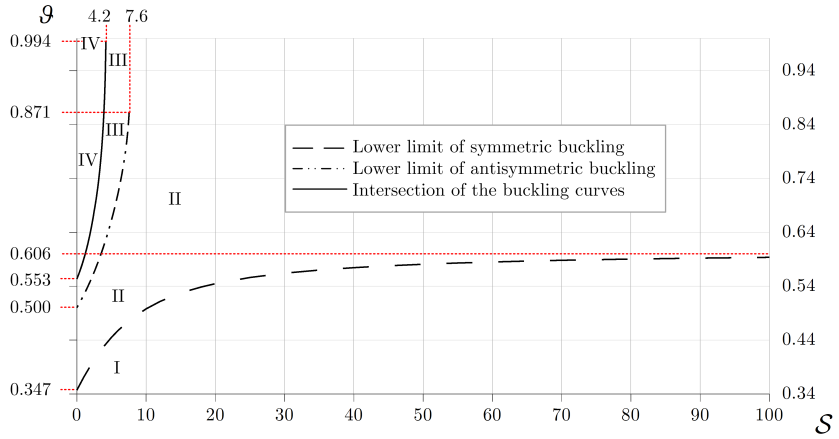

Figure 4. Typical buckling ranges when $m = 1\,000$.

equilibrium path as it will be shown later. Apart from the range limits, there are no any other differences as long as $\mathcal{S} \leq 4.2$. Passing this value results in the disappearance of the intersection point of the buckling curves, therefore antisymmetric buckling is only possible after symmetric buckling. Another limit of importance is $S = 7.6$, since above that, the bifurcation point vanishes. It can also be seen that as $\mathcal{S}$ approaches to infinity from below – i.e. the arch becomes fixed – the switch between no buckling and symmetric buckling can be found at $\vartheta = 0.606$. The results when $[\mathcal{S} = 0]$ $(\mathcal{S} \to \infty)$ are in a complete accord with what have been achieved in [20], [21]. This statement is valid for all the forthcoming results as well.

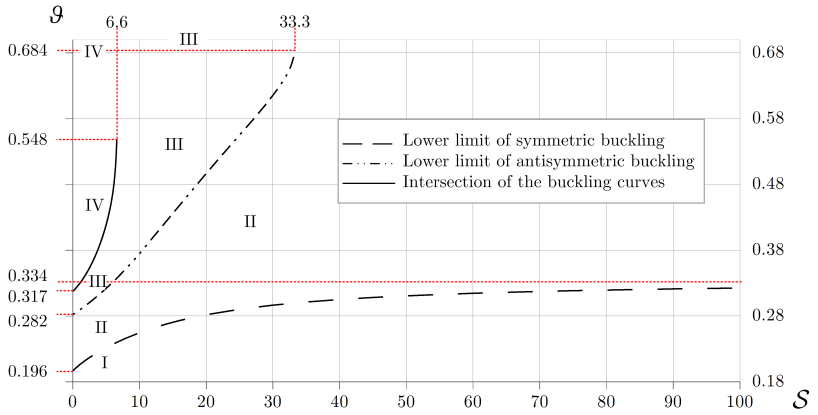

Figure 5. Typical buckling ranges when $m = 10\,000$.

The behavior of arches with $m = 10\,000$ is very similar to the former description – see Figure 5. This time an intersection point can be found up until $\mathcal{S} = 6.6$ and an upper limit for antisymmetric buckling until $\mathcal{S} \leq 33.3$. So these points show an

increase in $\mathcal{S}$ as m is increased. It is also noticeable that increasing m yields a decrease in all the typical buckling endpoints in ϑ.

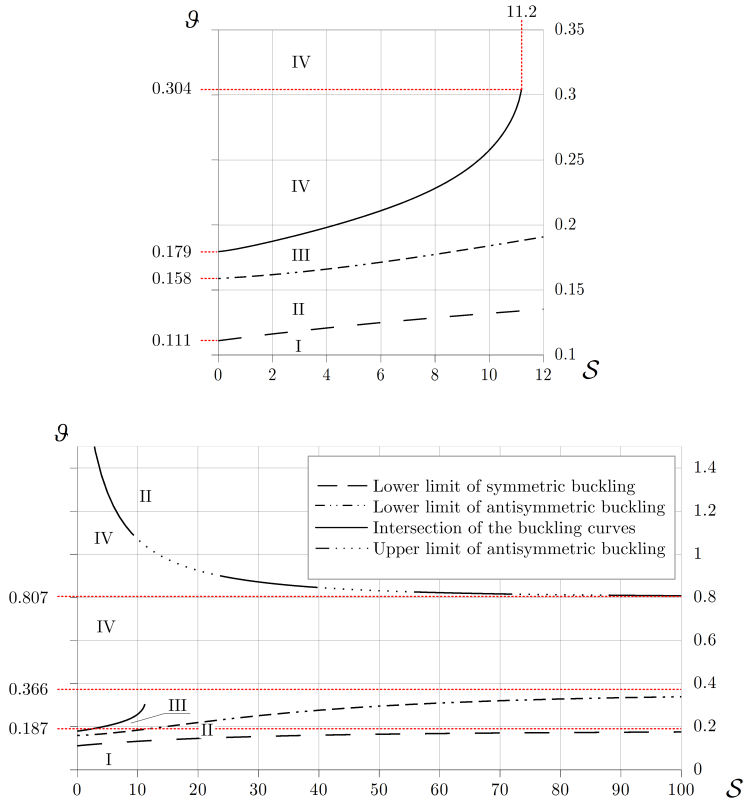

Figure 6. Typical buckling ranges when $m = 100\,000$.

More complex are the results in Figure 6 obtained for $m = 100\,000$, since the presence of an upper limit for antisymmetric buckling is experienced above $\mathcal{S}(\vartheta < 1.5) = 2.83$. Therefore, if $\mathcal{S} = 0 \ldots 2.83$ there is a range in which there is no buckling (I). It is followed by the range of symmetric buckling only (II). Then antisymmetric buckling comes after symmetric buckling (III). After that, for all included angles, the antisymmetric shape governs. However, for $\mathcal{S} = 2.83 \ldots 11.2$ after range (IV) the symmetric shape becomes again the dominant (II), since the possibility of antisymmetric buckling vanishes. A further increase in the spring stiffness yields the vanishing of the intersection point, so above range (I) the symmetric shape governs.

The characteristics of the curves valid for $m = 1\,000\,000$ in Figure 7 are very similar to that described in relation with $m = 100\,000$. So an increase in m results in a slight increase in the upper limit for antisymmetric buckling and a decrease in all other limits expressed in ϑ.

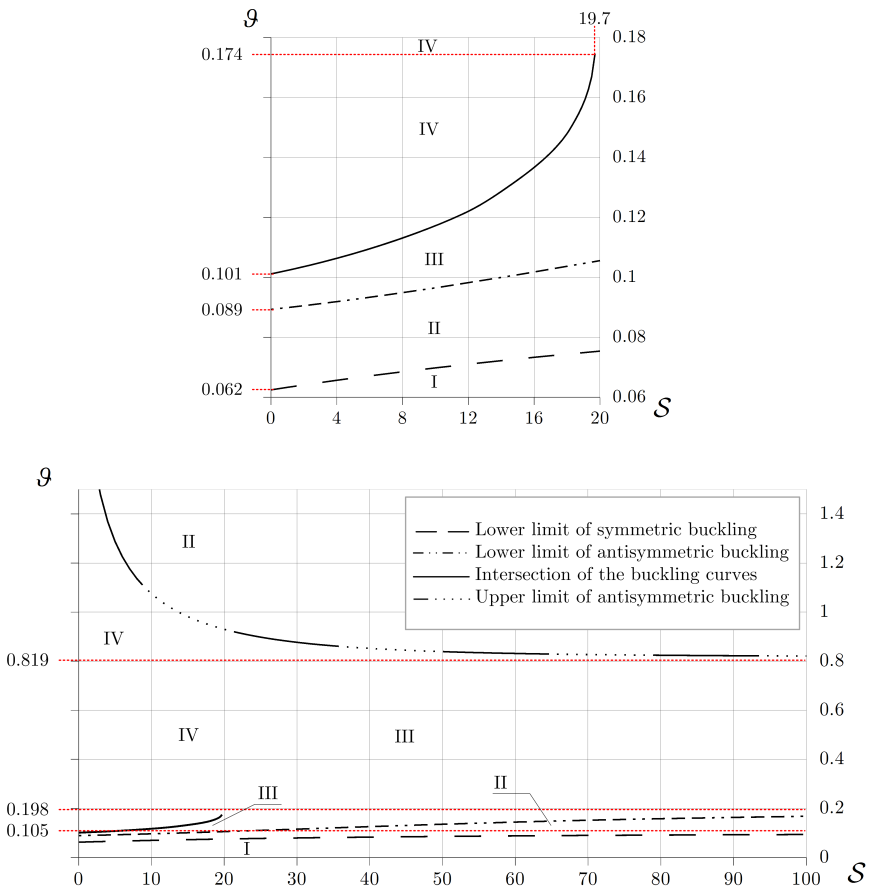

Figure 7. The typical buckling ranges when $m = 1\,000\,000$.

6.3. **Buckling curves.** In what follows, the governing buckling curves are drawn for four magnitudes of m. In each of these graphs, curves are presented for $\mathcal{S} = 0$ (pinned-pinned arch); $\mathcal{S} = 10^{20}$ (fixed-fixed arch with a very good accuracy) and $\mathcal{S} = 1$ (rotationally restrained arch) with the restriction that when both symmetric and antisymmetric shape is possible only the one, which comes prior in the load-deflection curve is plotted, since that is the dominant – see Section 6.4.

Antisymmetric buckling can be evaluated upon substitution of the critical strain for antisymmetric buckling from (47) into the averaged pre-buckling strain (40), therefore

$$\mathcal{P} = \left.\frac{-I_1 \pm \sqrt{I_1^2 - 4(I_0 - \varepsilon_{m\,cr\,anti})I_2}}{2I_2}\right|_{\chi^\vartheta = \mathfrak{F}} . \tag{61}$$

Here we get two solutions for the load but only the one in relation with the first bifurcation point is presented.

As for symmetric buckling we have two unknowns – the force and the critical strain. We also have two equations – one obtained from the averaged pre- (40) and one from the averaged post-buckling strain (57). Solving these simultaneously

$$\left[I_2\mathcal{P}^2 + I_1\mathcal{P} + I_0 - \varepsilon_m\right]\Big|_{\chi,\vartheta,\mathcal{S},m} = \left[J_2\mathcal{P}^2 + J_1\mathcal{P} + J_0\right]\Big|_{\chi,\vartheta,\mathcal{S},m} \tag{62}$$

leads to the lowest buckling load. In Figure 8, $m = 1\,000$. The lower limits for symmetric buckling are $\vartheta(\mathcal{S}=0) = 0.346$; $\vartheta(\mathcal{S}=1) = 0.371$ and $\vartheta(\mathcal{S}=10^{20}) = 0.606$. This buckling type is dominant for fixed-fixed arches throughout the whole interval while for the other two cases an intersection point was found with the corresponding antisymmetric curve at $\vartheta(\mathcal{S}=0) = 0.553$ and $\vartheta(\mathcal{S}=1) = 0.590$. Above these the antisymmetric buckling governs. It can therefore be seen that increasing the value of $\mathcal{S}$ results that the lower limit of symmetric buckling and the intersection point moves to the right in the scale with increasing corresponding buckling loads. It is also clear that arches with rotationally restrained ends can bear such loading levels, which are between the critical loads for pinned-pinned and fixed-fixed arches. It is generally quite a notable range in $\mathcal{P}$ so account for such restraints seems inevitable.

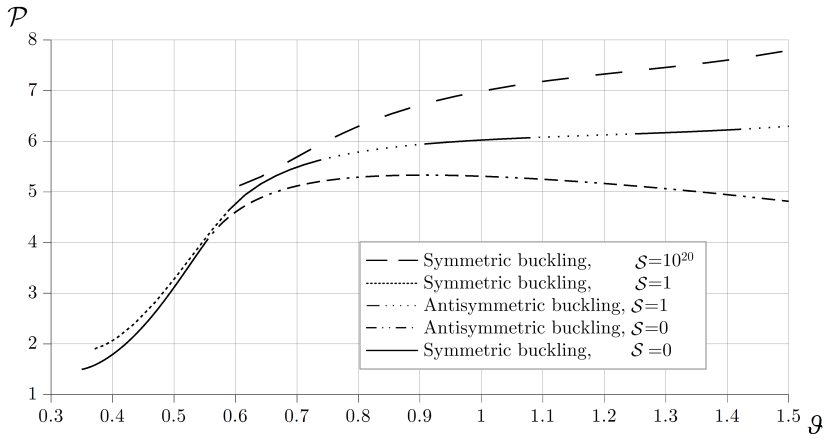

Figure 8. Buckling loads versus the semi-vertex angle when $m = 1\,000$.

Setting m to 10 000 yields what is shown in Figure 9. Now the lower endpoints for symmetric buckling are $\vartheta(\mathcal{S}=0) = 0.196$; $\vartheta(\mathcal{S}=1) = 0.205$ and $\vartheta(\mathcal{S}=10^{20}) = 0.334$ so the increase in m decreases this limit as it has already been pointed out in relation with Figure 5. It turns out that the intersection point in ϑ increases as the spring stiffness is increased: $\vartheta(\mathcal{S}=0) = 0.317$; $\vartheta(\mathcal{S}=1) = 0.328$. Above $\mathcal{S} = 6.6$, this point vanishes. It is also clear that the symmetric buckling curves of the two lowest stiffnesses run quite close compared to $m = 1\,000$. (This is the reason why this part is enlarged on the top part of the figure.) Above $\vartheta = 0.3$, they almost coincide. The critical load for any $\mathcal{S}$ is generally greater this time compared to the results when $m = 1\,000$.

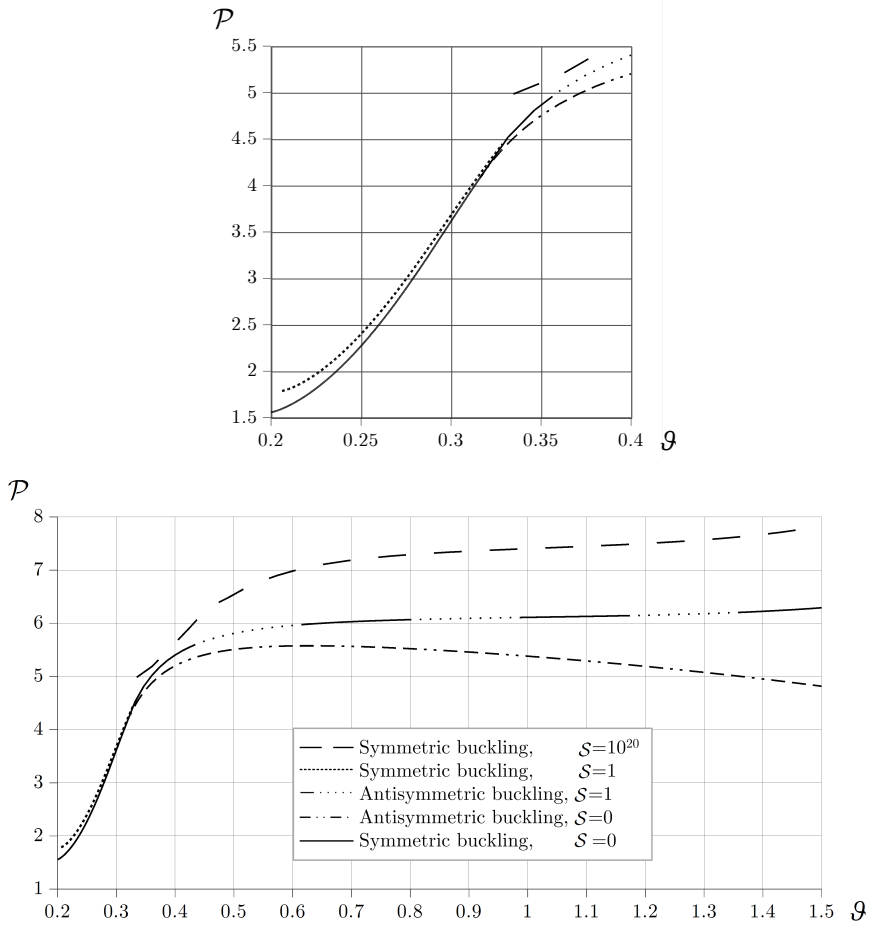

Figure 9. Buckling loads versus the semi-vertex angle when $m = 10\,000$.

In Figure 10, m is 100 000. The lower limit of symmetric buckling happens to decrease further but slowly: $\vartheta(\mathcal{S} = 0) = 0.111$; $\vartheta(\mathcal{S} = 1) = 0.113$ and $\vartheta(\mathcal{S} = 10^{20}) = 0.187$, while the intersection points occur at $\vartheta(\mathcal{S} = 0) = 0.179$; $\vartheta(\mathcal{S} = 1) = 0.182$. This time the symmetric curves are again closer to each other and the starting points of all the curves are closer to the origin.

With $m = 1\,000\,000$, we find that $\vartheta(\mathcal{S} = 0) = 0.062$; $\vartheta(\mathcal{S} = 1) = 0.063$ and $\vartheta(\mathcal{S} = 10^{20}) = 0.105$ are the lower limits for symmetric buckling and $\vartheta(\mathcal{S} = 0) = 0.101$; $\vartheta(\mathcal{S} = 1) = 0.102$ for the intersection point. This intersection point exists until $\mathcal{S} = 19.7$. The symmetric buckling curves for the two lowest stiffnesses coincide with a very good accuracy in their quite narrow interval in ϑ. Generally, the differences compared to $m = 100\,000$ are not that relevant when moving from $m = 1\,000$ to $m = 10\,000$.

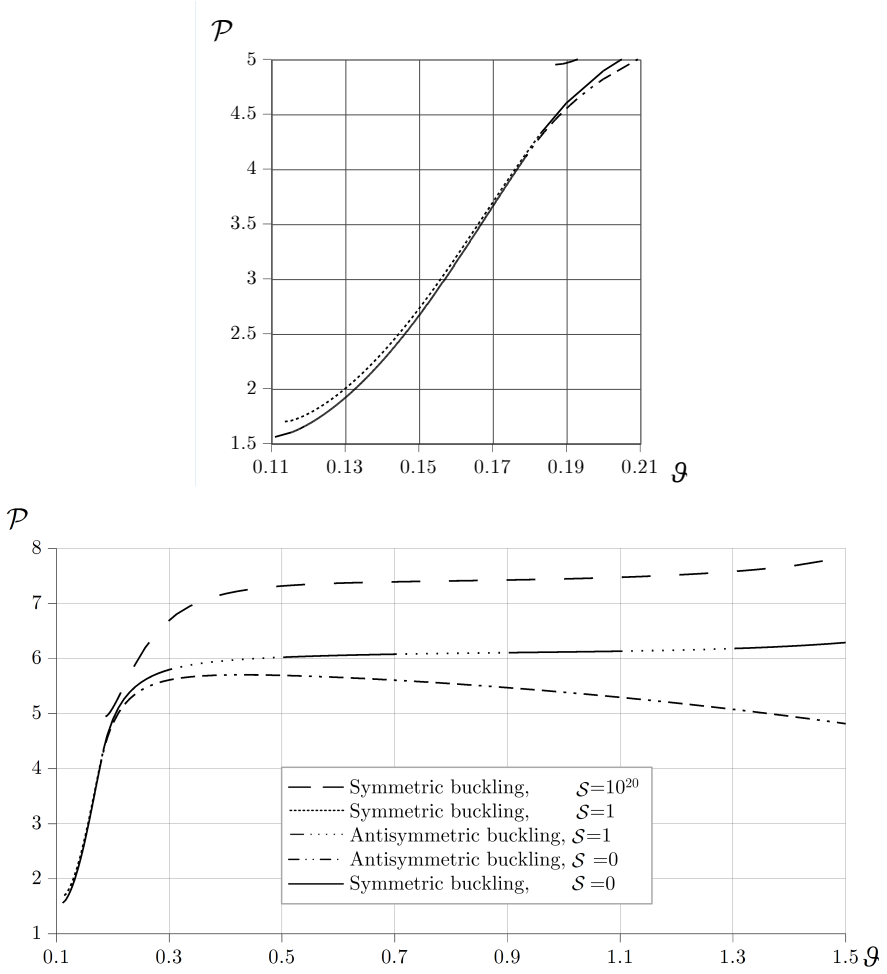

Figure 10. Buckling loads versus the semi-vertex angle when $m = 100\,000$.

It is clear from the corresponding figures that the presence of the springs have a huge effect on the buckling load. For instance, if $m = 1\,000\,000$ and $\vartheta = 1$ the critical dimensionless load varies between 5.4 and 7.5. This range becomes greater when the central angle is greater as it turns out.

The results of the new model for symmetric buckling are verified by finite element computations using Abaqus 6.7. The cross-section considered is rectangular with 0.01 $[m]$ width and 0.005 $[m]$ height and the Young's modulus is $2 \cdot 10^{11}$ $[Pa]$. $B22$ (3-node quadratic Timoshenko) beam elements and the Static,Riks step have been used to draw the load-deflection diagrams. Results are gathered in Table 4. It can be seen that the greatest differences (4.4%) are experienced when $m = 10^6$ and $\vartheta = 1.366$, so predictions of the new model for not so shallow arches also seem to be quite good.

This new model, anyway, generally yields lower critical loads except when $m = 10^3$ and $\vartheta = 0.641$.

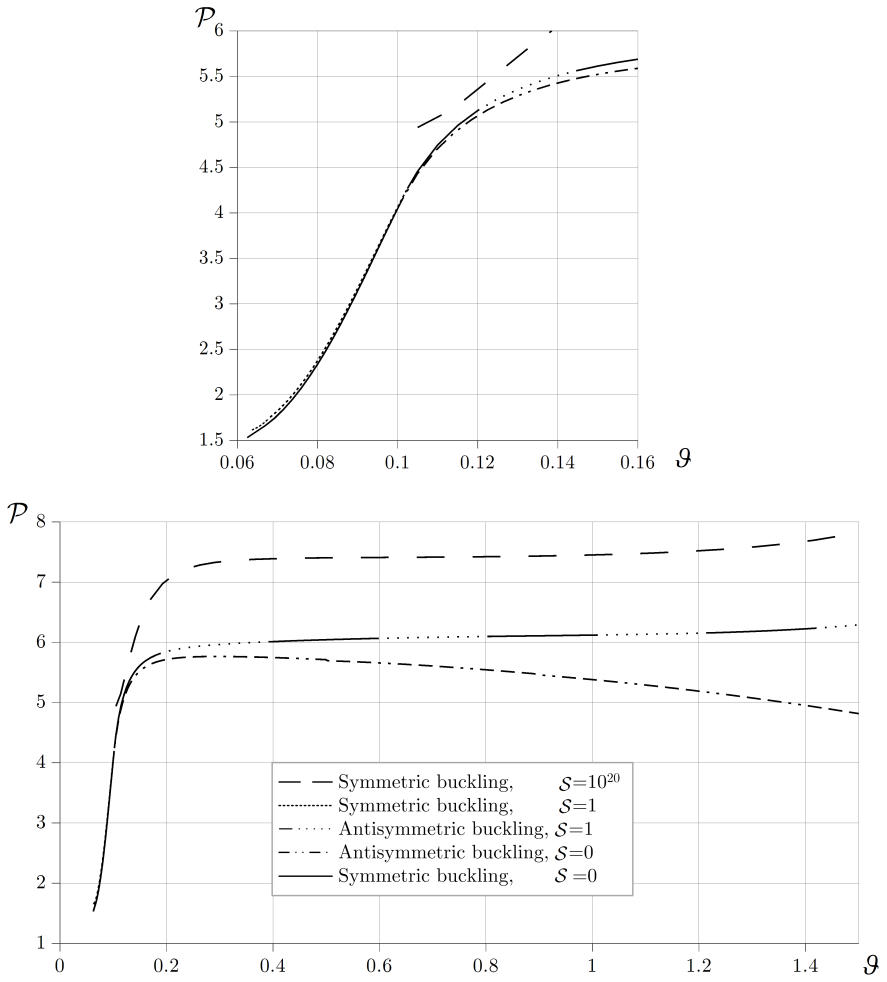

Figure 11. Buckling loads versus the semi-vertex angle when $m = 1\,000\,000$.

Table 4. Some control results regarding the symmetric buckling loads.

$\mathcal{S}$	m	ϑ	$\mathcal{P}_{\text{Abaqus}}$	$\mathcal{P}_{\text{New model}}$
$0/10/10^{20}$	10^3	0.641	4.98 / 5.03/5.09	5.23 / 5.26 / 5.29
$0/10/10^{20}$	10^3	1.052	6.78 / 6.83 / 6.99	6.70 / 6.86 / 7.09
$0/10/10^{20}$	10^3	1.416	7.48 / 7.51 / 7.71	7.36 / 7.43 / 7.62
$0/100/10^{20}$	10^6	0.289	6.75 / 7.20 / 7.38	6.69 / 7.14 / 7.32
$0/10/10^{20}$	10^6	0.782	6.98 / 7.18 / 7.52	6.76 / 6.99 / 7.42
$0/10/10^{20}$	10^6	1.366	7.58 / 7.70 / 7.98	7.26 / 7.39 / 7.64

6.4. **The primary equilibrium paths and the load-strain relationships.** In Figure 12 on the horizontal axis, the dimensionless displacement of the crown point W_{oC} is plotted against the dimensionless load $\mathcal{P}$ for arches with $m = 100\,000$. The former quantity is obtained by dividing the displacement (36) at $\varphi = 0$ by the rise of the arch:

$$W_{oC} = \frac{-W_o|_{\varphi=0}}{1 - \cos\vartheta}. \tag{63}$$

There are four central angles picked to represent the different path types when $\mathcal{S} = 1$ (continuous lines in the forthcoming figures). Results for $\mathcal{S} = 0$ (fine dashed lines), $\mathcal{S} = 15$ (dotted lines) and $\mathcal{S} = 10^{20}$ (dashed lines) are also included. When $\vartheta = 0.113$, the slope is always positive and there is neither limit point nor bifurcation point for the spring supported arches. This is also true for the fixed-fixed arch with, of course,

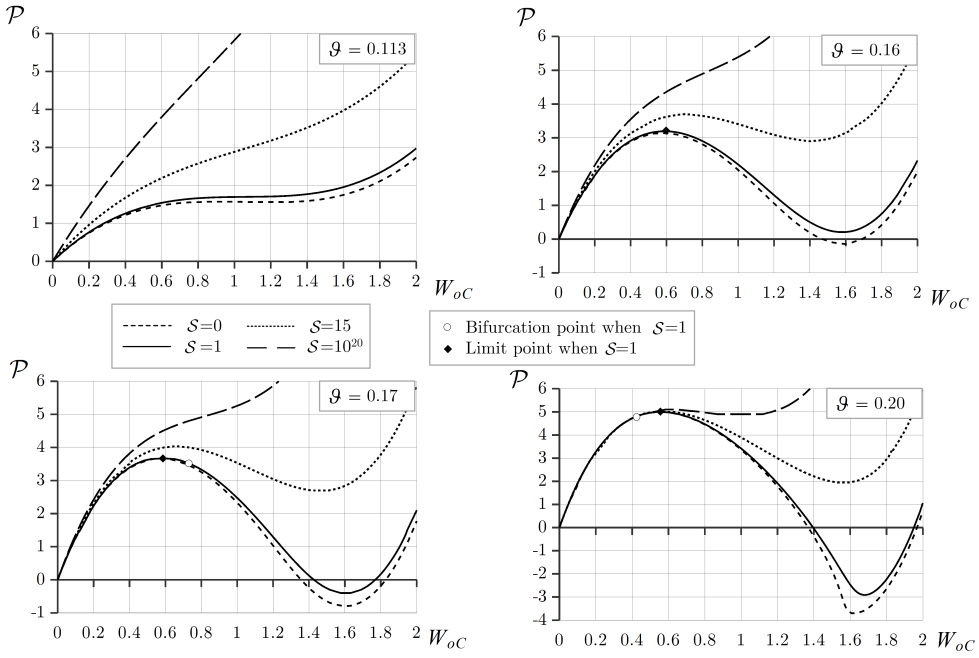

Figure 12. Dimensionless crown point displacement versus dimensionless load, $m = 100\,000$.

less displacement under the same load. However, for a stiff pin support, there appears a limit point. Increasing ϑ to 0.16 results in the appearance of a limit point for all but the fixed arch and the corresponding critical loads increase with $\mathcal{S}$. The fixed arch still has a positive tangent throughout but this curve generally runs closer to the others up until the first limit point on the curves for the restrained arches. At $\vartheta = 0.17$, there can be found a bifurcation point also but on the descending branch of the corresponding load-deflection curve for the pinned and restrained arches. Finally, for $\vartheta = 0.2$, there is a limit point in all four curves and these are quite close to each

other as well as all the first stabile branches. This time, and above this central angle, the two picked rotationally restrained and the pinned arches buckle antisymmetrically first, as the bifurcation point is located on the stabile branch, while fixed arches might still buckle symmetrically only.

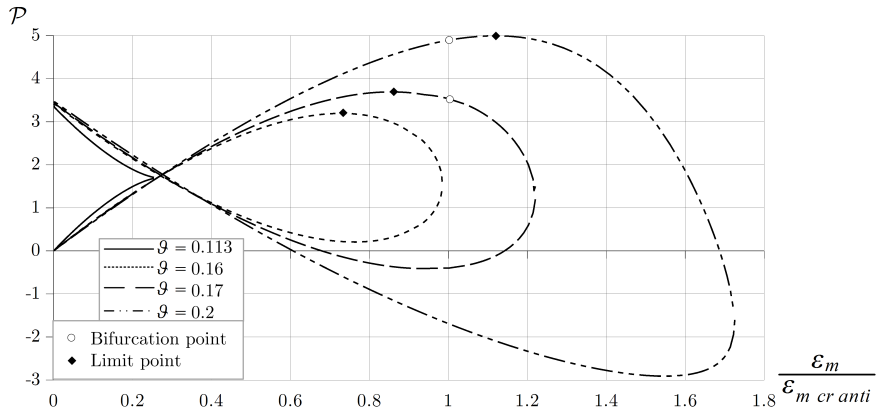

Figure 13. Typical load-strain relationships for $m = 100\,000$.

For $\mathcal{S} = 1$, the load-strain curves are drawn in Figure 13. On the horizontal axis the strain - critical strain ratio for antisymmetric buckling is measured. When $\vartheta = 0.113$, there are two different branches to which always a different $\mathcal{P}$ belongs. If $\vartheta = 0.16$, the branches intersect each other and a limit point also appears at which symmetric snap-through buckling occurs. However, the $\varepsilon_m/\varepsilon_{m\,cr} = 1$ ratio is not reached, so there is no bifurcation. Increasing ϑ to 0.17, we experience that a bifurcation point appears after the limit point. Finally, if ϑ is greater or equal with 0.2, the bifurcation point comes prior to the limit point, so the antisymmetric buckling shape dominates for such shallow arches under a central load. It is also remarkable that every time there are two branches. The first one always starts at the origin, while the second one commences around $3.3 - 3.5$ in $\mathcal{P}$, depending on the angle. There is an intersection point at $\varepsilon_m/\varepsilon_{m\,cr} \approx 0.27$ to which a loading level of $\mathcal{P} \approx 1.75$ belongs.

7. Conclusions

For rotationally restrained shallow arches with cross-sectional heterogeneity, a geometrically nonlinear model for the buckling analysis has been presented, partly on the basis of [17]. Nonlinearities were taken into account assuming the dominance of the rotation field. By using the principle of virtual work, we have derived the governing differential equations both for the pre-buckling and post-buckling state for arches under a central concentrated load and an arbitrary distributed load. Based on this achievement, the pre-buckling axial strain, as well as the post-buckling strain is constant on the centerline, when only a concentrated load is exerted at the crown

point. Heterogeneity appears in the formulation through the parameter $\chi(m)$. The equations of static equilibrium posses less neglects than the model derived and solved by Bradford et al. – see e.g., [15]; [17]. For this reason, the results computed by using the current model are more accurate even for greater central angles as well when they are compared to the previously cited articles. It should also be mentioned that for the rotation field the effect of the tangential displacement is neglected, which can cause erroneous predictions for deeper arches.

The evaluation process of the results are based on what Bradford et al. have used in their series of articles. We have presented how the different buckling limits and ranges are affected by the spring stiffness. It turns out that symmetrically supported shallow arches under a central load can buckle in an antisymmetric bifurcation mode with no strain increment at the moment of the stability loss, and in a symmetric snap-through mode, when there is a buckling strain. We have found, in an agreement with the earlier results, that an increase in $\mathcal{S}$ results in an increase of the typical buckling limits for any fixed m. However, as m increases, those limits show a decrease. Evaluation of the critical loads for three different spring stiffness is carried out. If $\mathcal{S} = 0$ and $\mathcal{S} \to \infty$, we retrieved the results valid for pinned-pinned and fixed-fixed arches – see [20], [21]. The rotational restraints can have a considerable effect on the critical load a shallow arch can bear. For the same arches, but with different spring stiffnesses, the maximum difference between the critical loads can reach up to 25% when $\vartheta \leq 0.8$ and up to 57% for greater central angles. The load-deflection curves are also affected by the rotational restraints as it has been presented.

Acknowledgements. This research was supported by the **European Union** and the **State of Hungary, co-financed by the European Social Fund** in the framework of TÁMOP 4.2.4.A/2-11-1-2012-0001 'National Excellence Program'.

The author would also like to express his gratitude to the unknown reviewers for their valuable and constructive comments.

Appendix A.1. Detailed manipulations

Calculation of the pre-buckling averaged strain. Integral (38) is divided into two parts. The first part is

$$\frac{1}{\vartheta}\int_0^{\vartheta} W_o \,\mathrm{d}\varphi = I_a + I_b\mathcal{P},$$

where

$$I_a = \frac{1}{\vartheta}\int_0^{\vartheta}\left(\frac{\chi^2-1}{\chi^2} + A_{11}\cos\varphi - \frac{A_{31}}{\chi^2}\cos\chi\varphi\right)\mathrm{d}\varphi = \frac{\chi^2-1}{\chi^2} + A_{11}\frac{\sin\vartheta}{\vartheta} - \frac{A_{31}}{\chi^3}\frac{\sin\chi\vartheta}{\vartheta}, \tag{A.1}$$

$$I_b = \frac{1}{\vartheta^2}\int_0^{\vartheta}\left(A_{12}\cos\varphi + A_{22}\sin\varphi - \frac{A_{32}}{\chi^2}\cos\chi\varphi - \frac{A_{42}}{\chi^2}\sin\chi\varphi\right)\mathrm{d}\varphi =$$

$$= \frac{1}{\vartheta^2}\left(A_{12}\sin\vartheta - A_{22}\cos\vartheta - A_{32}\frac{\sin\chi\vartheta}{\chi^3} + A_{42}\frac{\cos\chi\vartheta}{\chi^3} + A_{22} - \frac{A_{42}}{\chi^3}\right). \quad (A.2)$$

The other part is of the form

$$\frac{1}{\vartheta}\int_0^{\vartheta}\frac{1}{2}\psi_{o\eta}^2 \mathrm{d}\varphi = I_c + I_d\mathcal{P} + I_e\mathcal{P}^2\ . \quad (A.3)$$

Here

$$I_c = \frac{1}{2\vartheta}\int_0^{\vartheta}\left(B_{11}\sin\varphi + B_{31}\sin\chi\varphi\right)^2 \mathrm{d}\varphi = \frac{-1}{8\vartheta\chi\left(1-\chi^2\right)}\times$$
$$\times\left[B_{11}^2\chi\left(\sin 2\vartheta - 2\vartheta\right) + \frac{8B_{11}B_{31}\chi\left(\sin\chi\vartheta\,\cos\vartheta - \chi\sin\vartheta\,\cos\chi\vartheta\right)}{\left(1-\chi^2\right)} + B_{31}^2\left(\sin 2\chi\vartheta - 2\vartheta\chi\right)\right]. \quad (A.4)$$

To simplify the calculation it is advisable to decompose I_d:

$$I_d = \frac{1}{\vartheta^2}\int_0^{\vartheta} B_{11}\sin\varphi\left(B_{12}\sin\varphi + B_{22}\cos\varphi + B_{32}\sin\chi\varphi + B_{42}\cos\chi\varphi\right)\,\mathrm{d}\varphi +$$
$$+\frac{1}{\vartheta^2}\int_0^{\vartheta} B_{31}\sin\chi\varphi\left(B_{12}\sin\varphi + B_{22}\cos\varphi + B_{32}\sin\chi\varphi + B_{42}\cos\chi\varphi\right)\,\mathrm{d}\varphi = I_{d1} + I_{d2}\ , \quad (A.5)$$

where

$$I_{d1} = \frac{-B_{11}}{4\vartheta^2\left(1-\chi^2\right)}\left\{B_{12}\left(1-\chi^2\right)\left(\sin 2\vartheta - 2\vartheta\right) + B_{22}\left(1-\chi^2\right)\left(\cos 2\vartheta - 1\right) +\right.$$
$$\left. + 4B_{32}\left[\sin\chi\vartheta\,\cos\vartheta - \chi\cos\chi\vartheta\,\sin\vartheta\right] + 4B_{42}\left[\cos\vartheta\,\cos\chi\vartheta + \chi\sin\vartheta\,\sin\chi\vartheta - 1\right]\right\} \quad (A.6a)$$

and

$$I_{d2} = \frac{B_{31}}{4\chi\vartheta^2\left(1-\chi^2\right)}\left\{4\chi B_{12}\left[\chi\sin\vartheta\,\cos\chi\vartheta - \sin\chi\vartheta\,\cos\vartheta\right] +\right.$$
$$+ 4\chi B_{22}\left[\sin\vartheta\,\sin\chi\vartheta + \chi\cos\vartheta\,\cos\chi\vartheta - \chi\right] + B_{32}\left(1-\chi^2\right)\left[2\vartheta\chi - \sin 2\chi\vartheta\right] +$$
$$\left. + B_{42}\left(1-\chi^2\right)\left[1-\cos 2\chi\vartheta\right]\right\}\ . \quad (A.6b)$$

Moving on now to the calculation of I_e in (A.3), it is again worth decomposing the factor in question as

$$\begin{aligned} I_e =& \frac{1}{\vartheta^3}\int_0^{\vartheta}\left(B_{12}\sin\varphi + B_{22}\cos\varphi + B_{32}\sin\chi\varphi + B_{42}\cos\chi\varphi\right)\,B_{12}\sin\varphi\mathrm{d}\varphi + \\ &+\frac{1}{2\vartheta^3}\int_0^{\vartheta}\left(B_{12}\sin\varphi + B_{22}\cos\varphi + B_{32}\sin\chi\varphi + B_{42}\cos\chi\varphi\right)B_{22}\left(\cos\varphi\right)\,\mathrm{d}\varphi + \\ &+\frac{1}{2\vartheta^3}\int_0^{\vartheta}\left(B_{12}\sin\varphi + B_{22}\cos\varphi + B_{32}\sin\chi\varphi + B_{42}\cos\chi\varphi\right)B_{32}\left(\sin\chi\varphi\right)\mathrm{d}\varphi + \\ &+\frac{1}{2\vartheta^3}\int_0^{\vartheta}\left(B_{12}\sin\varphi + B_{22}\cos\varphi + B_{32}\sin\chi\varphi + B_{42}\cos\chi\varphi\right)B_{42}\left(\cos\chi\varphi\right)\,\mathrm{d}\varphi = \\ &= I_{e1} + I_{e2} + I_{e3} + I_{e4}\ . \end{aligned} \quad (A.7)$$

The four terms in this sum are

$$I_{e1} = \frac{B_{12}}{8\vartheta^3\left(1-\chi^2\right)}\left\{B_{12}\left(1-\chi^2\right)\left[2\vartheta - \sin 2\vartheta\right] + B_{22}\left(1-\chi^2\right)\left[1-\cos 2\vartheta\right] +\right.$$
$$\left. + 4B_{32}\left(\chi\sin\vartheta\,\cos\chi\vartheta - \cos\vartheta\,\sin\chi\vartheta\right) + 4B_{42}\left[1-\cos\vartheta\,\cos\chi\vartheta - \chi\sin\vartheta\,\sin\chi\vartheta\right]\right\}\ , \quad (A.8a)$$

$$I_{e2} = \frac{-B_{22}}{8\vartheta^3\left(\chi^2-1\right)}\left\{B_{12}\left(\chi^2-1\right)\left(\cos 2\vartheta - 1\right) - B_{22}\left(\chi^2-1\right)\left(\sin 2\vartheta + 2\vartheta\right) + \right.$$
$$\left. + 4B_{32}\left[\chi\cos\vartheta\,\cos\chi\vartheta + \sin\vartheta\,\sin\chi\vartheta - \chi\right] + 4B_{42}\left[\sin\vartheta\,\cos\chi\vartheta - \chi\cos\vartheta\,\sin\chi\vartheta\right]\right\}\,, \quad \text{(A.8b)}$$

$$I_{e3} = \frac{B_{32}}{8\chi\vartheta^3\left(1-\chi^2\right)}\left\{4B_{12}\chi\left[\chi\sin\vartheta\,\cos\chi\vartheta - \cos\vartheta\,\sin\chi\vartheta\right] + \right.$$
$$+ 4B_{22}\chi\left[\sin\vartheta\,\sin\chi\vartheta + \chi\cos\vartheta\,\cos\chi\vartheta - \chi\right] +$$
$$\left. + B_{32}\left(1-\chi^2\right)\left[2\vartheta\chi - \sin 2\chi\vartheta\right] + B_{42}\left(1-\chi^2\right)\left[1-\cos 2\chi\vartheta\right]\right\} \quad \text{(A.8c)}$$

and

$$I_{e4} = \frac{B_{42}}{8\vartheta^3\chi\left(\chi^2-1\right)}\left\{4B_{12}\chi\left[\cos\vartheta\,\cos\chi\vartheta + \chi\sin\vartheta\,\sin\chi\vartheta - 1\right] + \right.$$
$$+ 4B_{22}\chi\left[\chi\cos\vartheta\,\sin\chi\vartheta - \sin\vartheta\,\cos\chi\vartheta\right] + 2B_{32}\left(\chi^2-1\right)\sin^2\chi\vartheta +$$
$$\left. + 2B_{42}\left(\chi^2-1\right)\left[\chi\vartheta + \sin\chi\vartheta\,\cos\chi\vartheta\right]\right\}\,. \quad \text{(A.8d)}$$

With the knowledge of the previous integrals

$$I_0 = I_a + I_c\,, \qquad I_1 = I_b + I_d \quad \text{and} \quad I_2 = I_e \quad \text{(A.9)}$$

are the coefficients in (40).

Calculation of the averaged strain increment. Integrals J_a and J_b in

$$\frac{1}{\varepsilon_{mb}\vartheta}\int_0^\vartheta W_{ob}\mathrm{d}\varphi = J_a + J_b\mathcal{P} \quad \text{(A.10)}$$

are given below in closed forms:

$$J_a = \frac{1}{\vartheta}\int_0^\vartheta\left(\hat{D}_{01} + \hat{D}_{11}\cos\varphi + \hat{D}_{41}\cos\chi\varphi + \hat{D}_{51}\varphi\sin\chi\varphi\right)\mathrm{d}\varphi =$$
$$= \frac{1}{\chi^2\vartheta}\left[\chi^2\left(\hat{D}_{01}\vartheta + \hat{D}_{11}\sin\vartheta\right) + \hat{D}_{41}\chi\sin\chi\vartheta + \hat{D}_{51}\left(\sin\chi\vartheta - \chi\vartheta\cos\chi\vartheta\right)\right]\,, \quad \text{(A.11a)}$$

$$J_b = \frac{1}{\vartheta^2}\int_0^\vartheta\left(\hat{D}_{12}\cos\varphi + \hat{D}_{22}\sin\varphi + \hat{D}_{32}\sin\chi\varphi + \hat{D}_{42}\cos\chi\varphi + \hat{D}_{52}\varphi\sin\chi\varphi + \right.$$
$$\left.+\hat{D}_{62}\varphi\cos\chi\varphi\right)\mathrm{d}\varphi = \frac{1}{\chi^2\vartheta^2}\left[\chi^2\left(\hat{D}_{12}\sin\vartheta + (1-\cos\vartheta)\,\hat{D}_{22}\right) + \hat{D}_{52}\sin\chi\vartheta + \right.$$
$$\left. + (\cos\chi\vartheta - 1)\,\hat{D}_{62} + \chi\left((1-\cos\chi\vartheta)\,\hat{D}_{32} + \hat{D}_{42}\sin\chi\vartheta - \hat{D}_{52}\vartheta\cos\chi\vartheta + \hat{D}_{62}\vartheta\sin\chi\vartheta\right)\right]\,. \quad \text{(A.11b)}$$

As for the third integral in (57), let us recall formulae (37) and (55). Consequently, we get

$$\frac{1}{\vartheta\varepsilon_{mb}}\int_0^\vartheta W_o^{(1)}W_{ob}^{(1)}\mathrm{d}\varphi = J_2\mathcal{P}^2 + J_d\mathcal{P} + J_c, \quad \text{(A.12)}$$

in which

$$J_c = -\frac{1}{\vartheta}\int_0^\vartheta\left(E_{11}\sin\varphi + E_{41}\sin\chi\varphi + E_{51}\,\varphi\cos\chi\varphi\right)\left(B_{11}\sin\varphi + B_{31}\sin\chi\varphi\right)\mathrm{d}\varphi\,, \quad \text{(A.13a)}$$

$$J_d = -\frac{1}{\vartheta^2}\int_0^\vartheta\left(B_{11}\sin\varphi + B_{31}\sin\chi\varphi\right)\times$$
$$\times\left(E_{12}\sin\varphi + E_{22}\cos\varphi + E_{32}\cos\chi\varphi + E_{42}\sin\chi\varphi + E_{52}\varphi\cos\chi\varphi + E_{62}\varphi\sin\chi\varphi\right)\mathrm{d}\varphi -$$

$$- \frac{1}{\vartheta^2} \int_0^{\vartheta} (E_{11} \sin\varphi + E_{41} \sin\chi\varphi + E_{51}\, \varphi \cos\chi\varphi)\, (B_{12} \sin\varphi + B_{22} \cos\varphi + \\ + B_{32} \sin\chi\varphi + B_{42} \cos\chi\varphi)\, \mathrm{d}\varphi\,, \quad \text{(A.13b)}$$

$$J_2 = -\frac{1}{\vartheta^3} \int_0^{\vartheta} (B_{12} \sin\varphi + B_{22} \cos\varphi + B_{32} \sin\chi\varphi + B_{42} \cos\chi\varphi) \times \\ \times (E_{12} \sin\varphi + E_{22} \cos\varphi + E_{32} \cos\chi\varphi + E_{42} \sin\chi\varphi + E_{52}\varphi \cos\chi\varphi + E_{62}\varphi \sin\chi\varphi)\, \mathrm{d}\varphi\,. \quad \text{(A.13c)}$$

Observe that

$$J_0 = J_a + J_c; \qquad J_1 = J_b + J_d.$$

We would like to emphasize that the above integrals can all be given in closed forms. We omit them from being presented here as these are very complex. Any mathematical software, like Maple 16 or Scientific Work Place 5.5 can calculate these constants.

References

1. Bresse, J. A. C.: *Recherches analytiques sur la flexion et la résistance des piéces courbes*. Mallet-Bachelier and Carilian-Goeury at V^r Dalmont, Paris, 1854.
2. Hurlbrink, E.: Festigkeitsberechnung von röhrenartigen Körpen, die unter äusserem Druck stehen. *Schiffbau*, **9**(14), (1907-1908), 517–523.
3. Chwalla, E. and Kollbrunner, C. F.: Beiträge zum Knickproblem des Bogenträgers und des Rahmens. *Stahlbau*, **11**(10), (1938), 73–78.
4. Timoshenko, S. P. and Gere, J. M.: *Theory of Elastic Stability*. Engineering Sociaties Monograps, McGraw-Hill, 2nd edn., 1961.
5. Schreyer, H. L. and Masur, E. F.: Buckling of shallow arches. *Journal of Engineering Mechanics Divison, ASCE*, **92**(EM4), (1965), 1–19.
6. Dadeppo, D. A. and Schmidt, R.: Sidesway buckling of deep crcular arches under a concentrated load. *Journal of Applied Mechanics,ASME*, **36**(6), (1969), 325–327.
7. Dym, C. L.: Bifurcation analyses for shallow arches. *Journal of the Engineering Mechanics Division, ASCE*, **99**(EM2), (1973), 287.
8. Dym, C. L.: Buckling and postbuckling behaviour of steep compressible arches. *International Journal of Solids and Structures*, **9**(1), (1973), 129.
9. Szeidl, G.: *Effect of Change in Length on the Natural Frequencies and Stability of Circular Beams*. Ph.D Thesis, Department of Mechanics, University of Miskolc, Hungary, 1975. (in Hungarian).
10. Noor, A. K. and Peters, J. M.: Mixed model and reduced/selective integration displacment modells for nonlinear analysis of curved beams. *International Journal of Numerical Methods in Engineering*, **17**(4), (1981), 615–631.
11. Calboun, P. R. and DaDeppo, D. A.: Nonlinear finite element analysis of clamped arches. *Journal of Structural Engineering, ASCE*, **109**(3), (1983), 599–612.
12. Elias, Z. M. and Chen, K. L.: Nonlinear shallow curved beam finite element. *Journal of Engineering Mechanics, ASCE*, **114**(6), (1988), 1076–1087.
13. Wen, R. K. and Suhendro, B.: Nonlinear curved beam element for arch structures. *Journal of Structural Engineering, ASCE*, **117**(11), (1991), 3496–3515.

14. Pi, Y. L. and Trahair, N. S.: Non-linear buckling and postbuckling of elastic arches. *Engineering Structures*, **20**(7), (1998), 571–579.

15. Bradford, M. A., Uy, B., and Pi, Y. L.: In-plane elastic stability of arches under a central concentrated load. *Journal of Engineering Mechanics*, **128**(7), (2002), 710–719.

16. Pi, Y. L. and Bradford, M. A.: Dynamic buckling of shallow pin-ended arches under a sudden central concentrated load. *Journal of Sound and Vibration*, **317**, (2008), 898–917.

17. Pi, Y. L., Bradford, M. A., and Tin-Loi, F.: Non-linear in-plane buckling of rotationally restrained shallow arches under a central concentrated load. *International Journal of Non-Linear Mechanics*, **43**, (2008), 1–17.

18. Pi, Y. L. and Bradford, M. A.: Nonlinear analysis and buckling of shallow arches with unequal rotational end restraints. *Engineering Structures*, **46**, (2013), 615–630.

19. Plaut, R.: Buckling of shallow arches with supports that stiffen when compressed. *ASCE Journal of Engineering Mechanics*, **116**, (1990), 973–976.

20. Kiss, L. and Szeidl, G.: In-plane stability of pinned-pinned heterogeneous curved beams under a concentrated radial load at the crown point. *Technische Mechanik, Accepted for publication.*

21. Kiss, L. and Szeidl, G.: In-plane stability of fixed-fixed heterogeneous curved beams under a concentrated radial load at the crown point. *Technische Mechanik, under review.*